STRUCTURAL EVOLUTION AND FATIGUE PERFORMANCE OF LASER WELDED 30MnVS6/SAE 045 XLF JOINTS

A Thesis
Presented to
the Graduate School of
Clemson University

In Partial Fulfillment
of the Requirements for the Degree
Master of Science
Materials Science & Engineering

---

by
Robert Trahern Houliston
December 2017

Accepted by:
Dr. Marian Kennedy, Committee Chair
Dr. Vincent Blouin
Dr. Bahman Sahebkar

ABSTRACT

Characterization of microstructural evolution and fatigue performance of laser welded joints was studied between microalloyed 30MnVS6 and high strength low alloy SAE 045 XLF steels. These steel grades were selected for potential application in a prototype automatic gearbox to be utilized within automotive manufacturing. Parameters were varied using an Nd:YAG laser welding system which included laser power (1,670 – 1,730 W), workpiece speed (1,700 – 1,800 mm/min), and laser beam focal position (-0.05 – 0.05 mm). Based on the parameters selected, the welds were produced using an energy transfer of between 305 and 325 $J/mm^{0.5} \cdot s^{0.5}$. A 3-level factorial design of experiments was used to produce a total of 54 welded samples covering 27 different parameter combinations (sample types). Once samples were produced, visual examination of the weld surfaces was performed in order to inspect for visible defects such as spatter, cracks, or voids. During this assessment, weld spatter was present on all samples but no other defects were observed. Immersion ultrasonic non-destructive testing was conducted to identify regions of the weld which were most likely to contain sub-surface discontinuities. Metallurgical analysis was performed on 9 sample types manufactured using the most extreme parameter combinations (Phase I). The remaining 18 sample types were reserved for future testing (Phase II). Metallographic cross-sections were taken at the areas of interest identified by ultrasonic inspection which concluded that no cracking or voids were present. A study of material hardness and microstructural evolution across the welds was performed and then correlated to the parameters used for

the production of each sample. Vickers hardness testing of the 30MnVS6 and SAE 045 XLF base materials was measured at 255.3 HV and 169.3 HV, respectively. Hardness values increased to 439.0 HV in the weld solidification zone and further to 550.3 HV in the 30MnVS6 heat affected zone. Unidirectional, torsional fatigue testing at 3,500 N·m was conducted for 2 million cycles on five sample types manufactured using the most extreme power to speed ratios. This testing simulated conditions seen in automatic transmissions used in passenger cars. This testing failed to produce fractures within the welds or base materials which suggest that the alloys and parameters selected for the study could be successfully transferred to applications within the gearbox manufacturing industry. Recommendations for future research include the expansion of the selected parameter ranges to achieve energy transfer levels outside of the range of 275 to 435 $J/mm^{0.5} \cdot s^{0.5}$. It is anticipated that a more significant reaction in weld properties would be achieved and could allow for the study of potential weld failure modes within this system.

DEDICATION

To my parents, Brian and Candia, who gave me every opportunity to chase my dreams.

And to my wife, Mary, whose love and support has given me the fire to

pursue this journey.

ACKNOWLEDGEMENTS

Throughout this journey, I have had the privilege of working with many different groups who both believed in me and provided an overwhelming amount of support. When considering if to apply to a graduate program, my colleagues at US Engine Valve were some of the first voice their support and pushed me to pursue this opportunity. Lee, David, Gregg and the entire Quality Laboratory team: *Thank you for your support and encouragement.*

The support for the majority my graduate work came from the ZFTG family. To production, engineering, and quality departments, to the applications and testing group: *This all would not have been possible without your support*. Terry and Will: *I hope to be able to polish samples as well as you one day. Thank you for showing me how to pursue excellence in metallography*. Dr. Sahebkar: *Thank you for mentoring me through this process and providing insight on the internal procedures for making a graduate thesis happen*.

I would like to thank Dr. Kennedy and all my committee members. From providing details about the graduate programs offered with the Clemson University Department of Materials Science & Engineering through my thesis defense, you have guided me throughout this endeavor. Dr. Kennedy, Dr. Blouin, and Dr. Sahebkar: *I thank you all for your overwhelming support and patience during my graduate work and thesis research project.*

TABLE OF CONTENTS

Page

TABLE OF CONTENTS

Page

TABLE OF CONTENTS

Page

TABLE OF CONTENTS

Page

LIST OF FIGURES

LIST OF FIGURES

LIST OF FIGURES

Figure Page

LIST OF FIGURES

Figure Page

LIST OF TABLES

LIST OF TABLES

Table Page

Chapter One

Overview of Laser Beam Welding, Mechanics, and Applications

Throughout the automotive industry there is a need to join metal components [1.1–3]. Common process methods for joining metals include soldering, brazing and welding [1.4]. Inherent differences in these techniques (e.g. temperature ranges at which they operate, the use of filler metals, etc.) prevent any one of these processes from being used universally to join any combination of metal parts [1.4]. In welding, a relatively high temperature is used to melt small volumes of metal parts for joining [1.4,5]. The parts to be joined together are commonly referred to as the workpiece. This term can also refer to a single piece of metal influenced by a laser beam. Prior research has shown that the similarity or dissimilarity of the metals and welding parameters, such as the power transferred into the weld zone, will influence the resulting metal microstructure across the joint [1.1]. Typically, engineers focus on understanding how these microstructures transition across the weld zone between each base metal. The structural performance of welds are typically quantified, depending on the type of loading the weld would typically see in service, in the form of strength (e.g. tensile, torsional, fatigue, etc.) across the joint.

This study focused on understanding how the microstructures evolved in alloys joined using laser welding, during which a laser beam was used to melt small volumes of the respective metals. Removal of the laser beam from the melt led to the solidification and fusion between components. For alloys, particularly steel alloys, the cooling rate can have a significant impact on the properties and performance of the welds [1.6]. In this

work, we were focused on understanding how the laser power, welding speed, and focal position influenced the microstructure joints between 30MnVS6/SAE 045 XLF alloys.

To provide context of this study, the importance of joining dissimilar alloys to the materials community was highlighted in Section 1.1. We then described the current state of laser welding process knowledge along with historical context (Section 1.2). Finally, we discussed recent studies by other research groups in understanding how microstructures evolved in joints (Section 1.3) and summarize (Section 1.4). The experimental design of parameters and methodologies for this study were described in Chapter 2 and the results of the destructive and non-destructive characterization methods of the 30MnVS6/SAE 045 XLF joints were summarized in Chapter 3. The fatigue testing of the welds (Chapter 4) and discussion of potential future research pathways (Chapter 5) followed.

1.1 Considerations for the Joining of Dissimilar Metals

The welding of identical alloys is important throughout industry and is a means to products with relatively uniform material properties. This can be important in the mitigation of manufacturing difficulties when product design requires large or complex geometries. When increasingly complicated designs require different properties throughout a product, there is typically a need for the joining of dissimilar materials. This is frequently seen throughout the automotive industry in the form of demand for weight reduction and increased vehicle efficiency [1.2,3,7].

The similarity or dissimilarity of metals is typically determined by variance in their composition and microstructure. Calculations such as carbon equivalent for ferrous alloys can be used to predict a particular steel grade's response to welding based on quantities of its alloying constituents. Since welding requires the heating, melting, and resolidification of small volumes of the metals, phase change temperatures such as melting and boiling points, shown in Table 1.1, also influence the joining process [1.1,8,9]. Additionally, properties such as thermal conductivity also play a role (Table 1.1). Metals such as aluminum and copper are significantly more thermally conductive than others and, as a result, require a greater amount of energy in order to sustain a molten weld pool [1.1]. Dissimilar metal pairings could include alloys with distinct base metals, such as an aluminum alloy joined with a titanium alloy [1.1,8]. Metals can also be considered dissimilar if the chemical composition or the phases in the alloys are significantly distinct. These might include joining an austenitic and martensitic stainless steels [1.1,9]. The extent of which the metal compositions vary could often influence the type of joining process or techniques selected since the process would induce defects.

Table 1.1: Properties of metals which can influence weld zone formation [1.1].

Metal	**Melting Temperature (K)**	**Boiling Temperature (K)**	**Thermal Conductivity ($W \cdot m^{-1} \cdot K^{-1}$)**
Fe	1809	3133	78
Al	933	2793	238
Cu	1356	2833	397
Ni	1728	3188	89
Ti	1940	3558	22
Zn	693	1184	120
Mo	2888	4883	137
W	3673	5828	174
Zr	2125	4673	23
Nb	2740	5013	54

While there are more considerations in joining dissimilar metals than those with identical compositions, product designs often require this complexity [1.1]. While increased component complexity often means improved functionality, it can also involve benefits from reduced product cost. By being able to form joints between dissimilar metals, designers can incorporate cost savings by reserving the use of higher grade alloys for a component's critical features while more cost effective metals can be implemented elsewhere [1.1].

1.2 Overview of Laser Beam Welding Processes

Laser welding processes share various common aspects with other types of welding processes, including the input of energy into a workpiece followed by the fusion of the components. Initially, the metals to be joined together are placed in contact with each other. A laser beam is then used to melt the material in contact between the two workpieces. Upon removal of the laser beam, the molten metal solidifies and results in fusion between the components. The power of the laser beam plays an important role in the formation of the weld zone. Table 1.2 lists common types of laser welding systems used throughout industry [1.5].

This research will focus on neodymium-doped yttrium aluminum garnet (Nd:YAG) systems which have been shown to weld components within the automotive industry [1.2,3]. A comparison between the wavelengths of lasers is shown in Table 1.2. An inherent advantage of solid-state Nd:YAG lasers is their ability to emit light at wavelengths of approximately 1 μm which allows the light wave to be carried via

traditional fiber optic cables [1.5]. The ability for laser beams to be directed via fiber optic cables is highly beneficial throughout manufacturing industries as it enables welding operations to be performed via multi-axis robots [1.5]. This is not feasible for CO_2 lasers, which produce wavelengths of around 10 μm [1.5].

Table 1.2: Types and properties of various laser welding systems [1.5].

Laser Types	**Wavelength (μm)**	**Lasing Media**	**Average Power (kW)**
LD-Pumped Solid State Laser	≈ 1	Nd:YAG	13.5
Laser Diode (LD)	≈ 1	InGaAsP, etc.	10
Disk Laser	1.03	Yb^{3+}:YAG	16
Lamp-Pumped YAG Laser	1.06	Nd:YAG	7
Fiber Laser	1.07	Yb^{3+}:SiO_2	100
CO_2 Laser	10.6	CO_2-N_2-He gas mix	15

Typical solid state laser welding systems are comprised of three basic components: (1) a resonator which produces the laser beam, (2) the beam delivery system that include various combinations of lenses, mirrors, and fiber optic cables, and (3) a fixturing system for the workpiece(s) [1.5]. These components all have impacts on welding parameters used to join workpieces. Figure 1.1 depicts a schematic diagram of a typical YAG welding system, similar to that used for this study. The resonator, which generates the laser and supplies its power, is comprised of a pair of mirrors and the optical cavity [1.5]. Located inside the optical cavity are the arc lamp and Nd:YAG crystal which generate the laser beam. Once the laser beam is generated from the resonator it can be further manipulated via mirrors and lenses which influence beam spot size and focal position. The near-infrared wavelength of Nd:YAG lasers allow for the use of traditional fiber optic cables to direct the laser beam to the workpiece [1.5]. This

allows for the position of the laser beam to be varied. Movement of the workpiece relative to the laser is used to vary welding speed.

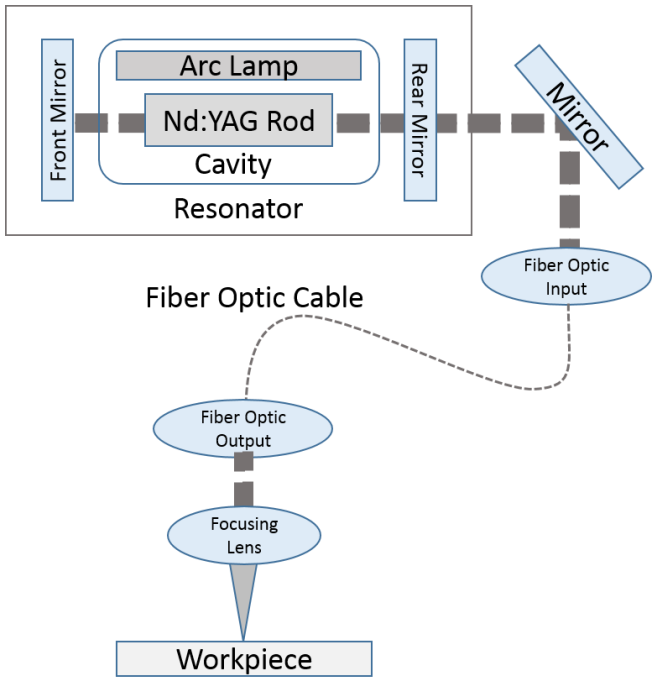

Figure 1.1: Schematic diagram of a basic solid-state Nd:YAG welding system [1.5].

Solid-state Nd:YAG lasers are able to operate in either pulsed or continuous wavelength modes of operation [1.5,10]. Pulsed wavelength processes, where laser power is rapidly fluctuated up to thousands of times per second, typically transfer less energy into the workpiece. This technique is useful in the precision joining of heat sensitive components, such as electrical components, jewelry, etc. [1.5]. Conversely, continuous wavelength modes can attain much higher power levels and are typically used for larger, more robust workpieces. In relatively older units, lamp-powered solid-state lasers were often used for welding applications; however, these units required high levels

of electrical power to operate and could typically achieve only 4% efficiency [1.5]. Modern systems use laser-diode pumping solid-state lasers, which not only output higher power levels, but demand lower electrical power input and can achieve between 30-60% efficiency [1.5].

In laser welding, two different types of welds can be formed by varying the amount of power transferred to the workpiece over time [1.5,10]. Lower laser power transferred into the joint can result in a conduction-type weld, where the energy input into the workpiece is only enough to melt metal at the surface where the laser beam is focused [1.5,10]. Alternatively, higher power levels transferred into the joint are able to achieve greater penetration depth into the workpiece and produce a keyhole-type weld [1.5,10,11]. In this thesis, the primary focus will be on keyhole-type welds whose mechanisms will be described below.

1.2.1 Mechanics of Keyhole Welding

Keyhole welds are formed from significantly greater penetration depths than those of conduction welds [1.5]. Once a sufficient amount of laser power is absorbed by the workpiece, a shallow pool of molten metal forms on the surface of the joint. Solidification of this liquid metal is typically sufficient for the production of a conduction weld. For deeper welds, additional power per area, typically a minimum of 10^6 W/cm^2, is required [1.1,4]. This will continue to heat the molten pool until it vaporizes and begins to rapidly expand [1.1,10,12]. This recoil pressure increases the depth of the molten pool into the workpiece [1.10]. As a metal gas plume forms, it interacts with the beam

creating a laser-induced plasma [1.10]. Formation of the vaporized metal and subsequent recoil pressure will result in a deep weld geometry as shown in Figure 1.2 . Recoil pressure supports the fluid metal lining the keyhole structure and prevents molten material from falling into the bottom of the keyhole [1.10]. Upkeep of the gas plume and the sustainment of recoil pressure during the welding process are critical factors in the weld's geometry [1.10].

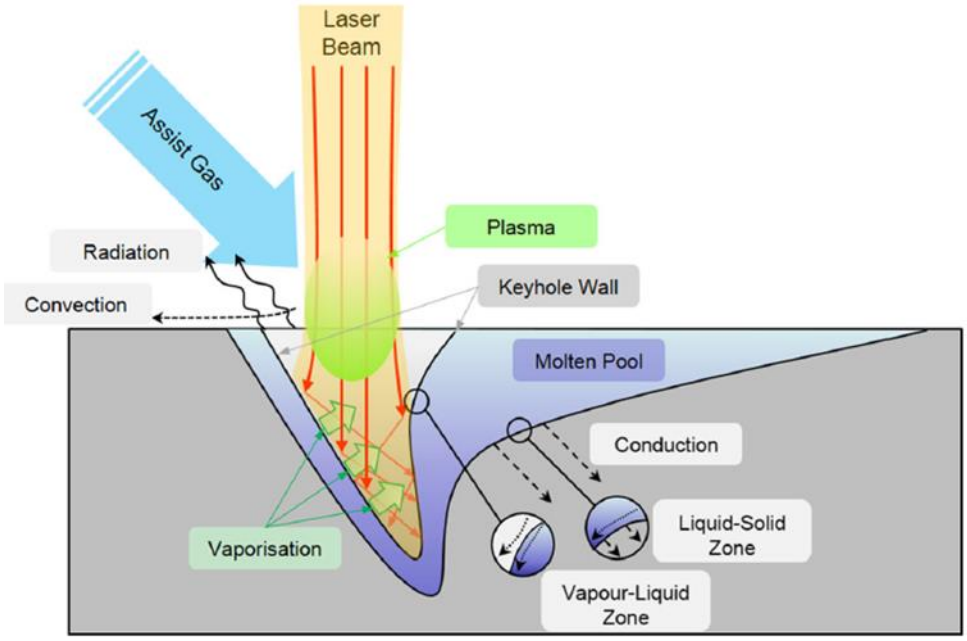

Figure 1.2: Cross-sectional diagram of a typical keyhole weld where the laser beam is travelling right to left [1.12]. In this diagram, the front keyhole wall is to the left of the laser beam. This figure was reprinted without permission.

An increase in welding speed can result in a more horizontal front keyhole wall (Figure 1.2) [1.10]. However, the drawback of increased welding speed is a shallower keyhole depth since less power is absorbed by the workpiece [1.10]. Conversely, stationary or low welding speeds will result in vertical keyhole walls that are

geometrically more difficult to sustain as the fluid keyhole walls are prone to collapse due to the low surface tension of the molten metal [1.10].

Supplementary techniques have been developed to further increase the stability of keyhole structures during slower welding speeds. For example, the implementation of inert gas jets has demonstrated effectiveness in supporting keyhole walls [1.10], particularly in situations where the front wall is vertically angled [1.13,14]. Furthermore, optimized use of assist gas jets resulted in a decrease in both porosity and spatter defects but was also observed to increase penetration depth and narrow the weld bead width [1.13,14].

1.2.2 Generation of Laser Welding Defects

In virtually all manufacturing industries, process cycle time has a profound influence on profitability. For most types of defects, their frequency of occurrence tends to be influenced by the balance between laser power and workpiece speed [1.10]. In the following section we will discuss the mechanisms behind some of the more common types of defects present in laser welding (porosity, spatter, and cracking) and how they can impact product quality.

1.2.2.1 Porosity Related to Keyhole Wall Collapse

The presence of weld porosity has been found to be detrimental to the overall strength and structural integrity of a workpiece [1.15]. For laser beam keyhole welding, the formation of porosity typically originates from the superheated metal vapor plume that produces the keyhole structure. Vapor from the superheated molten keyhole is

generated perpendicularly from the keyhole front wall as shown by Figure 1.2 [1.10]. This vapor flow, opposite of the welding direction, dynamically interacts with the solidifying keyhole rear wall and subsequently influences the plume's ejection angle[1.10]. Depending on the stability of the rear wall and the angle of the vapor flow off of the front wall, bubbles of the vapor plume and shielding gas can become trapped in the weld pool[1.10]. Another mechanism of porosity formation is associated with relatively deep and narrow keyholes produced by slower welding speeds. Here, additional recoil pressure must be produced in order to prevent the fluid keyhole walls from collapsing which can cause gasses to be trapped in the bottom of the keyhole [1.10,13].

1.2.2.2 Spatter Ejection from the Keyhole

Spatter is the formation of droplets of molten material that are ejected from the weld and can collect on the weld surface [1.2,4,5]. It is typically seen as aesthetically undesirable and can contaminate the optics of the laser welding system [1.2]. One of the mechanisms influencing welding spatter formation is the keyhole's front wall inclination angle [1.10,16–18]. As discussed earlier, recoil pressure is generated perpendicularly off of the front keyhole wall. If sufficient welding speed or laser power is present, front wall angle becomes more horizontal, the vapor plume coming off of the keyhole front wall will be directed towards the joint surface [1.16]. Conversely, spatter generated from a deeper, more vertical keyhole has to be ejected near-vertically in order to escape the weld. Here, the window for spatter to be ejected is much smaller and there is a higher chance of any spatter produced to be reincorporated into the keyhole wall [1.16]. In

Figure 1.3, high speed camera images taken of vapor plumes generated during YAG welding of X6CrNiTi18-10 stainless steel show that increasing laser power influences the angle of the vapor plume and amount of spatter ejected from the keyhole [1.18]. These images were captured by using a secondary illumination laser which was aimed at the vapor plume [1.18]. A pass-band filter was then used which prevented all light wavelengths, except for that of the illumination laser, from being recorded [1.18]. On the right, a higher vapor plume angle is visible in addition to spatter droplets escaping from the weld keyhole. Although the differences between the two images in Figure 1.3 are achieved by varying laser power, similar results can be achieved by increasing welding speed [1.17,18].

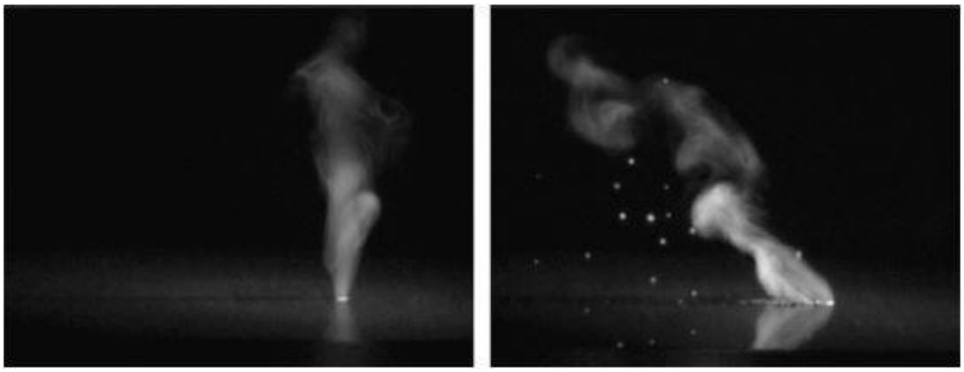

Figure 1.3: High-speed images taken of two Yb:YAG laser weld vapor plumes produced in X6CrNiTi18-10 stainless steel at 1.5kW (left) and 3.5kW (right). The welding direction in both images is left to right. Here, the vapor plume exhibits a change in angle and amount of spatter produced when varying laser power [1.18]. These images were reprinted without permission.

1.2.2.3 Solidification Related Cracking

Cracking is another defect type commonly associated with welding processes. According to the American Welding Society, cracking can be defined as, sharp-tipped fractures categorized by a high length to width ratio [1.19]. Cracking caused during the welding process can be categorized into two groups: hot cracking and cold cracking. Like most defects, both types of cracking are structurally detrimental to the product; however, each type of cracking can happen for different reasons and at different times.

Hot cracking occurs during the solidification process and will result in cracks being immediately present in the welded joint [1.4,19]. Weld solidification cracking occurs in the weld fusion zone during the end of the solidification process [1.4]. Two conditions must be met in order for weld solidification cracking to occur [1.4]. First, a significant enough amount of material strain as a result of the negative volume change during solidification must be present [1.4]. Additionally, the materials being welded must possess a brittle enough microstructure that is susceptible to cracking at elevated temperatures [1.4]. If ample internal stresses are present during the cooling period, which exceed the elasticity limits of the material at that particular temperature, the conditions for hot cracking have been achieved.

Cold cracking is also known as delayed cracking due since fractures typically propagate after solidification and complete cooling of the weld has concluded [1.20]. Cracking may not initiate in a product until after the component is in service, eliminating any reasonable opportunity to detect the defect via non-destructive methods such as eddy

current or ultrasonic testing. Factors typically present in materials susceptible to cold cracking include a microstructure with low toughness properties and significant residual stresses [1.20]. The presence of diffusible hydrogen can also play a major role in cold cracking but does not necessarily have to be present [1.20].

1.2.3 Characterization of Alloy Weldability

The ease of which alloys can be welded is described as their weldability [1.19]. One method often used to predict the weldability of a ferrous metal is to calculate its carbon equivalent. The magnitude of this factor has been used to predict hardenability of the heat affected zone and susceptibility to cold cracking of specific steel alloys [1.21]. Although this calculation does not consider the mixing of dissimilar steel grades into a single joint, it can help predict the reaction of each alloy individually. While there are many carbon equivalent formulae, they all are weighted averages taking into account various alloying elements which contribute to hardenability in heat affected zones and susceptibility to cold cracking [1.4,21]. These equations do not take into account non-compositional factors such as thermal conductivity, microstructural phases, or grain size but generally focus on the hardening capacity of ferrous alloys based on their composition [1.22]. These formulae consider carbon content along with other elements including manganese, chromium, molybdenum, and vanadium [1.4,21,22]. As there are many varying viewpoints on the impact of alloying constituents on weld stability, there is no universally acceptable relationship that governs all welding models. All carbon equivalent equations should be used more as guidance tool when selecting ferrous alloys

or predicting their reaction during welding. One version of the formula is that proposed by Yurioka et al. and is as follows:

$$CE_N = C + A(C) \cdot \left\{ \frac{Si}{24} + \frac{Mn}{6} + \frac{Cu}{15} + \frac{Ni}{20} + \frac{Cr+Mo+Nb+V}{5} + 5B \right\} \quad 1.1$$

where $A(C) = 0.75 + 0.25\ tanh\{20(C-0.12)\}$ [1.23]. This this particular formula considered to be a useful weldability index in a variety of steel types [1.24]. Application of these factors are typically used to determine whether ferrous alloys should be heated prior to or following during the welding process. It is common practice for steel grades with carbon equivalents greater than 0.35 to be preheated in order to mitigate the risk of cold cracking and excessive hardness [1.4]. When considering the studied alloys, 30MnVS6 and SAE 045 XLF, they each have a carbon equivalent of 0.60 and 0.12, respectively.

1.3 Results from Previous Laser Welding Research

Studies involving the welding of identical, similar, and dissimilar metal components have been reported on. In this section, we will summarize key findings.

1.3.1 Welding Studies Involving Similar Alloys

In order to understand how laser welding can impact the microstructure and properties in welds, it is first important to understand how joints of a single material or composition respond to varying welding parameters. We will discuss the research studies listed in Table 1.3.

Table 1.3: Referenced studies conducted involving pieces with identical compositions. We refer to these as welds of similar materials.

Primary Author	Material	Test Setup	Citation
Yoo, Y.-T.	S45C	Single Piece	[1.11]
Tadamalle, A. P.	AISI 304L	Single Piece	[1.25,26]
Jokar, M.	ST 14	Single Piece	[1.27]
Coelho, R. S.	S500MC	Butt Joint	[1.28]
Tenner, F.	X6CrNiTi18-10	Lap Joint	[1.18]
Brock, C.	S235	Lap Joint	[1.17]
Malek Ghaini, F.	ST 14	Single Piece	[1.29]
Liu, J.	SUS 301L	Lap Joint	[1.30]

1.3.1.1 Influence of Energy Transfer on Weld Geometry

In Section 1.2.1, deep laser weld production was linked to the ability to maintain a molten keyhole within the workpiece. One critical aspect in the production of a laser weld is that the front wall inclination of the keyhole may vary as it travels along the weld path [1.5,10]. By varying the speed at which the laser and workpiece move relative to one another, the front wall angle of the still-molten material can be manipulated [1.5,10].

Additionally, the amount of power transferred to the workpiece will directly affect the recoil pressure within the keyhole, further affecting its front wall inclination [1.5,10]. Achievement of the balance between speed and power is critical in the production of welds without the presence of spatter or void defects [1.5,10,17,18].

Supporting the theory that laser power and workpiece speed together have a significant impact on weld geometry, Y.-T. Yoo et al. [1.11] conducted welding trials using a continuous wave Nd:YAG system in order to determine an optimal power to speed ratio. These trials were conducted on a single piece of S45C steel. Use of a single piece of material, as opposed to separate parts in a joint configuration, was often used to study the reaction of a single material type [1.11,25–27,29]. This likely negated any effects that could potentially be caused interface imperfections between the two mating surfaces. Tests were conducted at three different laser powers with all showing a consistent inversely proportional relationship between welding speed and the achieved penetration depth (Figure 1.4) [1.11]. A variable for effective heat input, Q_{eff}, was defined as:

$$Q_{eff} = \frac{P}{\sqrt{V}} \tag{1.2}$$

where P is laser power and V is welding speed. Yoo showed that an effective heat input range from 275 to 435 J/mm$^{0.5}$·s$^{0.5}$, as displayed in Figure 1.5, produced a defect free welding range for this particular system[1.11]. Above this effective heat input range hot cracking and porosity defects were observed while below this range void defects were observed.

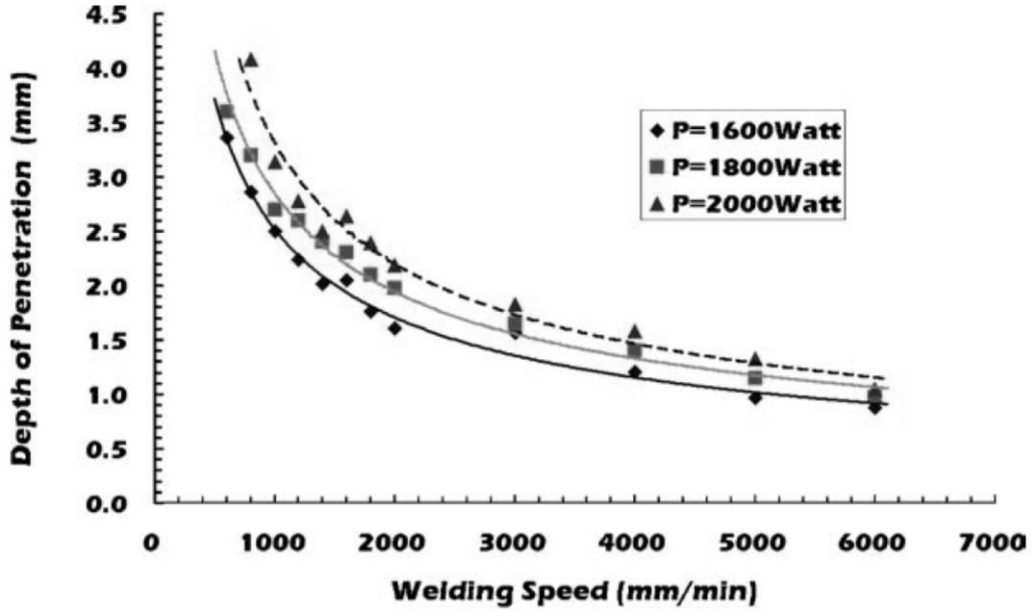

Figure 1.4: Y.-T. Yoo et al. suggested that welding speed is inversely proportional to depth of penetration [1.11]. This figure was reprinted without permission.

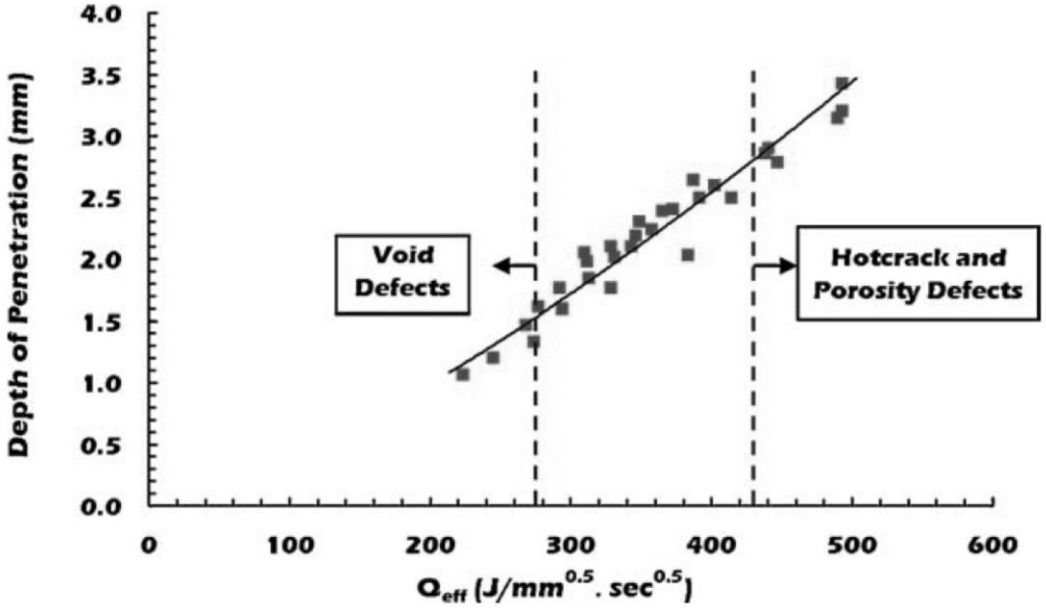

Figure 1.5: Testing revealed a direct relationship was derived between the effective heat input (Q_{eff}) and the depth of penetration. A range of effective heat inputs were found to produce welds without defects such as voids or hot cracks [1.11]. This figure was reprinted without permission.

Studies by A. P. Tadamalle et al. [1.25] and Malek Ghaini et al. [1.29] used an Nd:YAG laser system on 304L austenitic stainless steel and St14 steel, respectively, with the aim of determining which process parameters had the greatest effect on weld pool geometry. Unlike the studies performed by Yoo et al. [1.11], these studies used a pulsed laser delivery rather than a continuous beam. Comparable results with regards to a relationship between the energy transferred into the workpiece and the weld penetration depth were observed. Similar to the effective heat input variable proposed by Yoo, Tadamalle and Malek Ghaini focused on energy density into the workpiece. Here, unlike in a continuous wave laser system, transferred energy density could be broken down further by considering factors such as pulse duration and time between pulses [1.25,26,29]. Despite these differences, the relationship between energy transfer and penetration depth was still evident (Figure 1.6) [1.25].

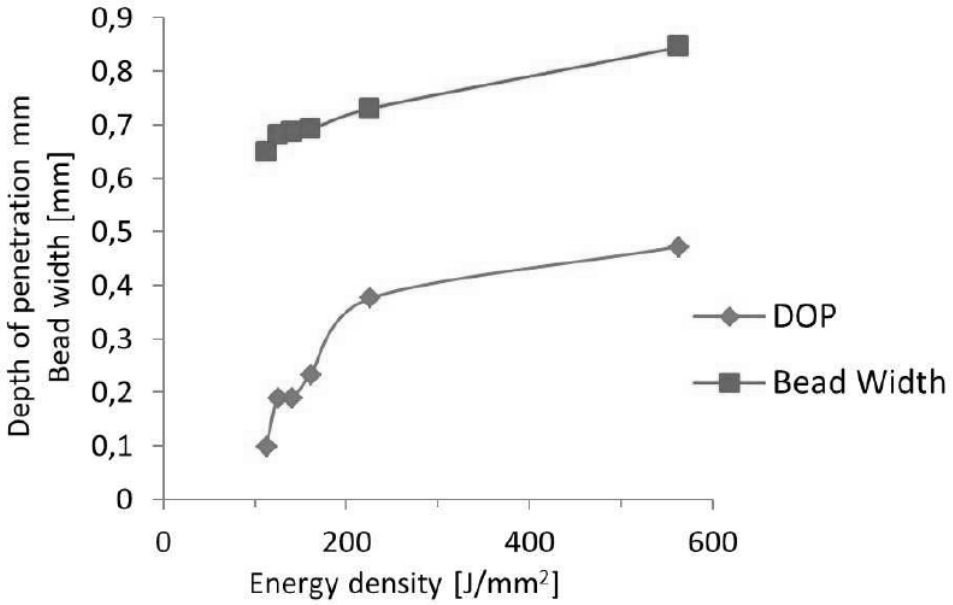

Figure 1.6: Using a pulsed Nd:YAG laser welding system on a single piece of AISI 304L stainless steel, Tadamalle et al. demonstrated the relationship between depth of penetration (DOP) and weld bead width to energy density [1.25]. This figure was reprinted without permission.

1.3.1.2 Shielding Gas Influence on Weld Geometry

In addition to energy input into a workpiece other factors such as shielding gas composition have been investigated [1.27]. In a study by Jokar et al., the use of pure argon was compared to argon mixed with up to 25 % carbon dioxide. As shown in Figure 1.7, relatively small additions of carbon dioxide to the inert argon shielding gas decreased the area and depth to width ratio of welds; however, higher additions of carbon dioxide increased the weld area and depth to width ratio [1.27]. An increase in plasma temperature was also observed following a similar trend to that of the depth to width ratio observed with relation to increasing percentages of carbon dioxide (Figure 1.7) [1.27]. It

was postulated that an iron oxide film may have formed on the surface of the weld pool which allowed for a more efficient absorption of energy from the laser beam [1.27].

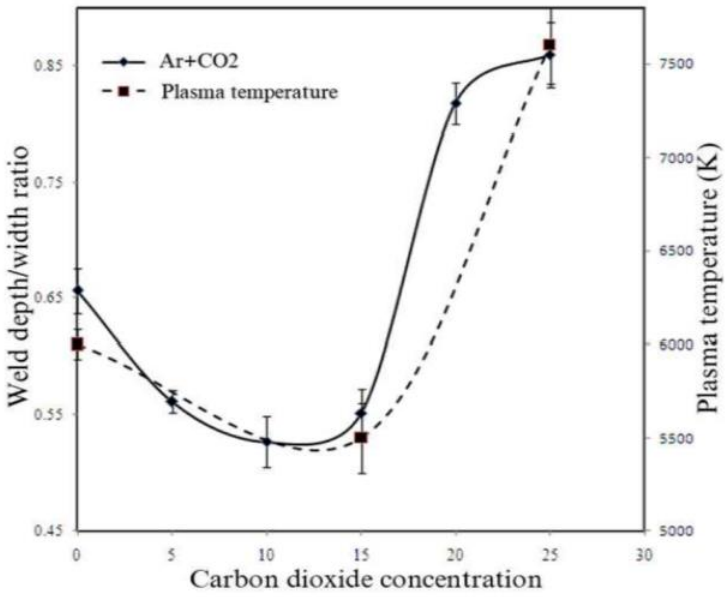

Figure 1.7: Influence of carbon dioxide additions to argon shielding gas on weld depth to width ratio and plasma temperature during Nd:YAG welding of a ST 14 low carbon steel plate [1.27]. This figure was reprinted without permission.

1.3.1.3 Pre-/Post-heating Influence on Laser Welds

In a study performed by Coelho et al. [1.28], the use of an induction heating system both before and after the laser beam welding process was used to manipulate the heating and cooling times of the weld. It was found that induction heating of the pieces allowed for an extended cooling period across the critical temperature range of 800 to 500 ºC during welding. Responses to this variable was assessed by observation to changes in weld microstructure and hardness. Here, welds were produced using a CO_2 laser welding system on a S500MC high strength low alloy steel.

Table 1.4: Cooling times (s) from 800 to 500 ºC of S500MC after the laser welding process for samples which underwent (A) no induction heat treatment, (B) pre-heating only, (C) post-heating only, and (D) both pre- and post-heating [1.28].

Sample Name	Top Side Cooling Time (s)	Bottom Side Cooling Time (s)
A	1.2	1.2
B	6.0	5.5
C	5.2	0.8
D	17.0	18.0

Table 1.4 shows the various cooling times from 800 to 500 ºC for various induction heating setups. The combination of induction heating the joint before and after welding allowed for the longest cooling time. The S500MC alloy tested in this study exhibited non-equilibrium bainitic and martensitic phases when welded with no induction heating process [1.28]. With the addition of an induction heating process before and after welding phases present in samples included various forms of ferrite including acicular (α_{ac}), polygonal (α_{pf}), and allotriomorphic (α_{af}) [1.28]. In conjunction with the reduced amounts of martensite and bainite observed, samples manufactured using longer cooling times exhibited a less significant hardness increase in the welded regions relative to samples with shorter cooling time as shown in [1.28]. Contrary to the lower hardness values in the welded regions employing slowest cooling rates, as shown in Figure 1.8, the author found that residual stress levels were still significant [1.28].

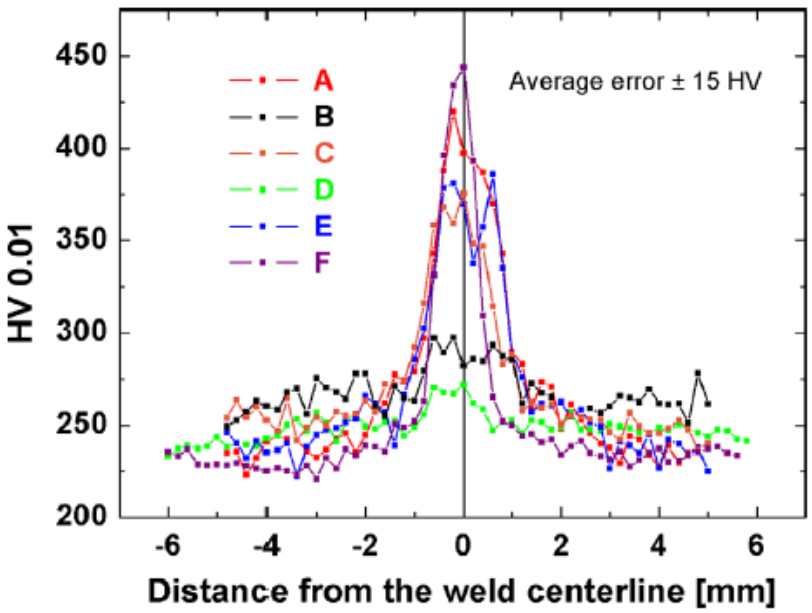

Figure 1.8: Hardness profiles across the welds produced as described by the nomenclature used in Table 1.4. Here, samples B and D exhibited the lowest hardness values through the centerline of the weld. Additional samples, E and F, were tested which involved post weld annealing and use of an Nd:YAG laser, respectively [1.28]. This figure was reprinted without permission.

1.3.2 Welding Studies Involving Dissimilar Alloys

While laser welding research involving similar workpiece compositions is important in better understanding the joining process, the study of dissimilar joint compositions enables the design of more complex components [1.1]. Although laser welding thermally affects a relatively small portion of the workpiece, mismatches in phase transformation temperatures, thermal conductivity, and expansion coefficients can still result in the degradation of weld properties [1.1]. Review of literature (Table 1.5) suggests that parameters which influence the welding of similar materials also impact the joining of dissimilar alloys.

Table 1.5: Referenced studies conducted involving dissimilar material applications. All dissimilar alloy systems listed are butt-joints.

Primary Author	Material A	Material B	Citation
Tomashchuk, I.	AA5754	Ti6Al4V	[1.8]
Berretta, J. R.	AISI 304	AISI 420	[1.9]
Rossini, M.	TWIP	22MnB5	[1.31]
	TWIP	DP	
	TWIP	TRIP	
	DP	22MnB5	
	DP	TRIP	
Cam, G.	AISI 316	St 37	[1.32]
Cui, Q. L.	DP	HSLA	[1.33]
Anawa, E. M.	AISI 316	AISI 1008	[1.34]

1.3.2.1 Energy Transfer via Offset Laser Positions

Laser welding studies of dissimilar base metals, such the aluminum and titanium alloys analyzed by Tomashchuk et al. [1.8], demonstrate that joining processes are still possible. The solidus temperature of AA5754 is almost 1200 K lower than that of Ti6Al4V, which forces the aluminum to remain in the liquid state much longer than that of the titanium alloy. Furthermore, the boiling point of the aluminum alloy is approximately 100 K higher than the solidus temperature of the titanium alloy, adding to the complexity of the scenario. Tomashchuk et al. determined via energy-dispersive x-ray spectroscopy (EDS) welded samples with lower tensile strength exhibited the presence of a contact interface where intermetallic Ti-Al phases were prominent [1.8]. As shown by in Figure 1.9, they achieved their best results by welding below 10 m/min and shifting the laser beam towards the AA5754 material [1.8]. Using these parameters, they

were able to achieve a narrower contact interface with fewer brittle intermetallic layers present [1.8].

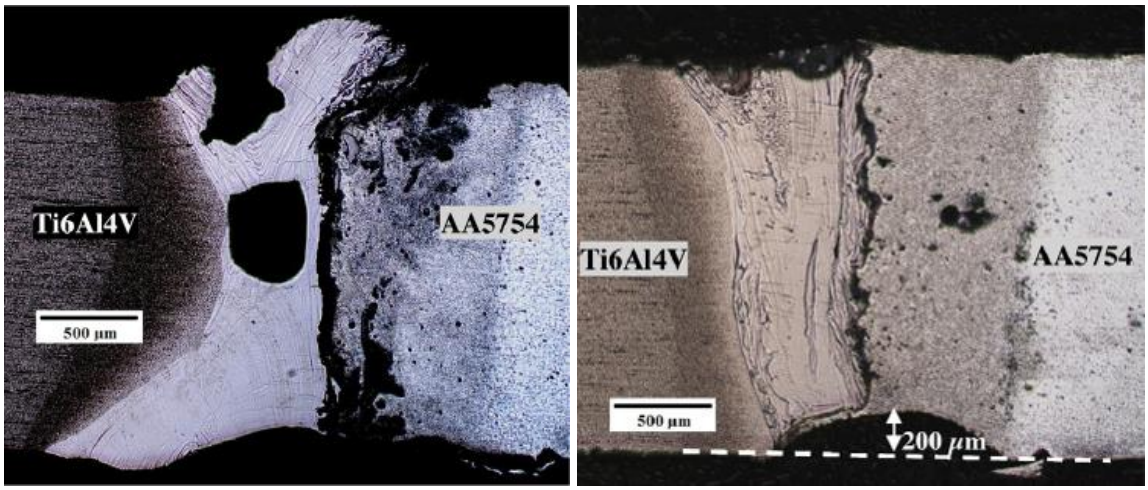

Figure 1.9: Cross-sections of various Ti6Al4V/AA5754 welds [1.8] showing: a 0.2mm shift towards the Ti6Al4V material (left) and a 0.2mm shift towards the AA5754 material (right). These images were reprinted without permission.

Different from dissimilar base metals studied by Tomashchuk, Berretta et al. studied laser welding parameter influence on dissimilar stainless steel alloy grades [1.9]. Here, AISI 304 austenitic stainless steel was joined to AISI 420 martensitic stainless steel by varying laser position relative to the joint location [1.9], similar to the methodology used by Tomashchuk [1.8]. Table 1.7 shows the tensile testing results performed by Berretta et al. as well as the fracture location of the samples [1.9]. In contrast to the work by Tomashchuk where the highest tensile levels were obtained by shifting the laser position to the aluminum alloy [1.8], the highest tensile strength values were obtained by not shifting the laser position from the joint [1.9].

Table 1.6: Tensile test results of pulsed Nd:YAG between AISI 304 and AISI 420 using offset laser positions [1.9].

Sample Type	Maximum Load (kN)	Yield Load (kN)	Deformation (%)	Fracture Location
AISI 304 (no weld)	687.9 ± 1.2	281.0 ± 8.0	89.6 ± 1.5	n/a
AISI 420 (no weld)	679.6 ± 2.8	428.7 ± 11.3	24.8 ± 0.8	n/a
0.2mm to AISI 304	152.9 ± 4.4	-	0.59 ± 0.07	Weld
0.1 mm to AISI 304	414.8 ± 17.1	283.4 ± 2.2	6.3 ± 0.9	Weld
No Offset	679.5 ± 1.9	295.3 ± 1.6	50.5 ± 0.3	Base Material
0.1 mm to AISI 420	598.6 ± 12.0	291.4 ± 0.4	24.3 ± 2.1	Weld
0.2 mm to AISI 420	326.5 ± 12.9	285.4 ± 0.8	2.2 ± 0.4	Weld

According to studies performed by both Tomashchuk and Berretta, it can be concluded that offset laser positions have been seen to influence weld strength [1.8,9]. When the dissimilar metals to be joined have significant property differences (e.g. phase change temperatures, thermal conductivity, etc.) offset laser welding positions can suppress the formation of phases detrimental to tensile strength. Conversely, in pairings of dissimilar alloy grades of the same base material category (e.g. AISI 304 and AISI 420) it was found that offset laser positions was always detrimental to weld tensile strength.

1.3.2.2 Joining of Dissimilar Automotive Steel Alloys

Laser welding research focusing specifically on steels commonly used throughout the automotive industry has been performed by Rossini et al. [1.31]. Here, joint combinations using twinning induced plasticity (TWIP) steel, transformation induced plasticity (TRIP) steel, dual phase steel, and 22MnB5 hot stamping boron steel were analyzed. These selected alloys were of interest throughout the automotive industry for various reasons such as dual phase steels, which are a commonly selected alloy group for

use in automotive body paneling [1.31]. TRIP alloys are often used for frame rail and engine cradle applications and hot stamping boron steels for use as A-pillars, B-pillars, or cross beams [1.31]. Additional emphasis was placed on the study of TWIP steels in dissimilar material welds as they exhibit high strength and ductility, ideal for shock-absorbing applications such as bumpers, but have proven difficult to weld in previous studies [1.31]. The ability to successfully join the aforementioned alloy types could potentially lead to opportunities for vehicle weight reduction and crashworthiness [1.31].

The performance the welds under tensile loading was performed for each of the welded material combinations. By comparing the ultimate tensile strength of the welds at the location at which the failure occurred, Rossini et al. were able to determine that the weld zone was not always the weakest point [1.31]. This was further shown by the fracture location of the DP/22MnB5 and DP/TRIP welds which failed in the dual phase base material. Alternatively, in all welds produced using TWIP steel, failure occurred within the fusion zone. Consistent with the compositional differences discussed (TWIP steel containing more carbon and manganese), joints using the TWIP steel were the only samples observed to fracture within the fusion zone during tensile testing [1.31].

Table 1.7: Tensile testing results of the welded material combinations produced. Here, yield strength (YS), ultimate tensile strength (UTS), elongation at failure (e_f), and the region in which the weld fractured were recorded [1.31].

Welded Joint	UTS (MPa)	e_f (%)	Fracture Region
TWIP/22MnB5	620	3	Fusion Zone
TWIP/DP	410	0.5	Fusion Zone
TWIP/TRIP	500	1	Fusion Zone
DP/22MnB5	875	18	DP Side
DP/TRIP	850	22	DP Side

Additional work was performed on the laser welding of dissimilar ferrous alloys by G. Cam [1.32] and Q. Cui [1.33]. Here, the primary focus of the studies involved the phases present due to the cooling rates following the welding process. This was studied through a combination of investigations into the microhardness of localized regions throughout the welds as well as microstructural evaluation and determination of fatigue life. In both studies, the interaction between the dissimilar alloys was not only studied, but the reaction of welds produced using the same material was also studied.

Though the research aim of both studies was similar, they diverged in the means which they determined fatigue strength. Cam et al. proceeded by producing three-point bend samples which were then notched and pre-cracked in the different regions of the weld in order to study how each region reacted to applied loads [1.32]. In later research, Q. Cui's approach was more traditional with regards to determining fatigue life of the samples produced. Here, butt-configuration welds were produced, and then transversely sectioned to produce a series of tensile specimens which were then fatigue tested at various load amplitudes [1.33]. Multiple conclusions were able to be derived from the fatigue data obtained, as shown by Figure 1.10. With regards to fatigue testing of welded joints between similar alloys, DP980 welds lasted longer than those produced using HSLA steel at stress amplitudes greater than 200 MPa [1.33]. When tested at stress amplitudes below 200 MPa, the opposite was observed with HSLA steel welds outlasting those of the DP980 alloy [1.33]. Dissimilar material welds produced using both the DP980 and HSLA steels were seen to have the lowest fatigue strength with fractures initiating at the interface between the fusion zone and DP980 material [1.33]. The

fracture was observed to have then propagated through the hardest region of the heat affected zone as identified via Vickers indentation testing [1.33].

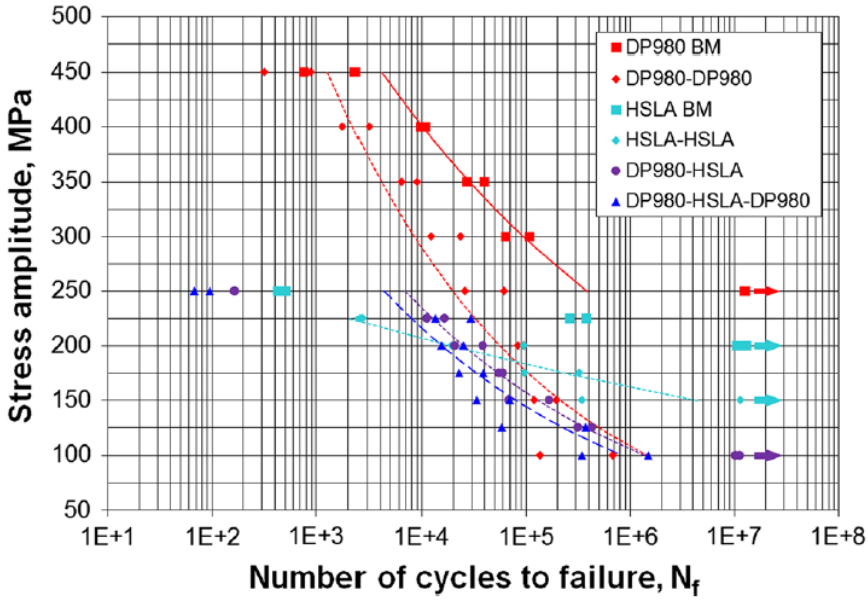

Figure 1.10: S-N curved produced by Q. Cui et al. [1.33] between welds using various combinations of dual phase (DP980) and high strength low allow (HSLA) steels. This figure was reprinted without permission.

1.3.2.3 Experimental Design Approaches in Welding

Experimental design approaches have been useful in determining relationships between process parameters and weld properties. Previously, J. Liu et al. performed a full factorial design of experiment on a SUS301L austenitic stainless steel lap joint using a continuous wave Nd:YAG welding system [1.30]. Input variables included laser power, welding speed, irradiation angle, and focal distance. Responses to these variables were documented with regards to weld width, depth of penetration, and shear strength.

A similar, multivariable design of experiment setup was employed by E. M. Anawa et al. [1.35]. Unlike the study performed by Liu [1.30], this considered laser power, workpiece velocity, and focal position were at five levels. Additionally, this research studied the welding of dissimilar alloys. Here, sample welds were manufactured from 316 stainless steel with a 1009 low carbon steel in a butt-joint configuration [1.35]. Again, laser power and workpiece speed were found to have the most significant impact on weld geometry.

1.4 Conclusions

In this section the motivations and considerations regarding the joining of similar and dissimilar alloys were described. Following this an overview of typical laser welding systems and processes was provided in order to provide context for this study. Finally, prior research was discussed in order to highlight key findings related to the joining of both similar and dissimilar metals.

1.5 References

[1.1] Z. Sun and J.C. Ion: *J. Mater. Sci.*, 1995, vol. 30, pp. 4205–14.

[1.2] A. Ribolla, G.L. Damoulis, and G.F. Batalha: *J. Mater. Process. Technol.*, 2005, vol. 164–165, pp. 1120–7.

[1.3] K.-M. Hong and Y.C. Shin: *J. Mater. Process. Technol.*, 2017, vol. 245, pp. 46–69.

[1.4] D.L. Olson, ed.: in *ASM Handbook: Welding, Brazing, and Soldering*, vol. 6, ASM Intl, 1993, pp. 229–48, 756–76, 1083–5.

[1.5] S. Katayama: in *Handbook of Laser Welding Technologies*, Woodhead Publishing Limited, 2013, pp. 3–15, 47–72.

[1.6] B.L. Bramfitt and B.S. Corporation: *Met. Handb. Desk Ed. Second Ed.*, 1998, pp. 153–73.

[1.7] E. Schubert, M. Klassen, I. Zerner, C. Walz, and G. Sepold: *J. Mater. Process. Technol.*, 2001, vol. 115, pp. 2–8.

[1.8] I. Tomashchuk, P. Sallamand, E. Cicala, P. Peyre, and D. Grevey: *J. Mater. Process. Technol.*, 2015, vol. 217, pp. 96–104.

[1.9] J.R. Berretta, W. de Rossi, M. David, M. Das Neves, I. Alves De Almeida, N. Dias, and V. Junior: *Opt. Lasers Eng.*, 2007, vol. 45, pp. 960–6.

[1.10] R. Fabbro: *Woodhead Publ. Ser. Electron. Opt. Mater.*, 2013, pp. 47–72.

[1.11] Y.-T. Yoo, D.-G. Ahn, K.-B. Ro, S.-W. Song, H.-J. Shin, and K. Im: *J. Mater. Sci.*, 2004, vol. 39, pp. 6117–9.

[1.12] G. Pastras, A. Fysikopoulos, C. Giannoulis, and G. Chryssolouris: *Int. J. Adv. Manuf. Technol.*, 2015, vol. 78, pp. 723–36.

[1.13] K. Kamimuki and T. Inoue: *J. Laser Appl.*, 2002, vol. 14, pp. 136–45.

[1.14] R. Fabbro: *J. Phys. D. Appl. Phys.*, 2010, vol. 43, pp. 1–9.

[1.15] R.F. Ashton, R.P. Wesley, and C.R. Dixon: *Weld. Res. Suppl.*, 1975, pp. 95–8.

[1.16] R. Fabbro, S. Slimani, I. Doudet, F. Coste, and F. Briand: *J. Phys. D. Appl. Phys.*, 2006, vol. 39, pp. 394–400.

[1.17] C. Brock, F. Tenner, F. Klämpfl, R. Hohenstein, and M. Schmidt: *Phys. Procedia*, 2013, vol. 41, pp. 539–43.

[1.18] F. Tenner, C. Brock, F. Klämp, and M. Schmidt: *Opt. Lasers Eng.*, 2015, vol. 64, pp. 32–41.

[1.19] American Welding Society (AWS) A2 Committee: *AWS A3.0M/A3.0:2010 Standard Welding Terms and Definitions*, 2009.

[1.20] H.J. Yi, Y.J. Lee, J.Y. Kim, and S.S. Kang: *J. Mech. Sci. Technol.*, 2011, vol. 25, pp. 2185–93.

[1.21] T. Kasuya and N. Yurioka: *Weld. Res. Suppl.*, 1993, pp. 263–8.

[1.22] Ş. Talaş: *Mater. Des.*, 2010, vol. 31, pp. 2649–53.

[1.23] N. Yurioka, H. Suzuki, S. Ohshita, and S. Saito: *Weld. J.*, 1983, vol. 62, pp. 147–53.

[1.24] N. Yurioka: *ISIJ Int.*, 2001, vol. 41, pp. 566–70.

[1.25] A.P. Tadamalle, Y.P. Reddy, and E. Ramjee: *Adv. Prod. Eng. Manag.*, 2013, vol. 8, pp. 52–60.

[1.26] A.P. Tadamalle, Y.P. Reddy, E. Ramjee, and V.K. Reddy: *Adv. Prod. Eng. Manag.*, 2014, vol. 9, pp. 128–38.

[1.27] M. Jokar, F. MalekGhaini, M.J. Torkamany, and M. Sheikhi: *Iran. J. Phys. Res.*, 2014, vol. 14, pp. 41–6.

[1.28] R.S. Coelho, M. Corpas, J.A. Moreto, A. Jahn, J. Standfuß, A. Kaysser-Pyzalla, and H. Pinto: *Mater. Sci. Eng. A*, 2013, vol. 578, pp. 125–33.

[1.29] F. Malek Ghaini, M.J. Hamedi, M.J. Torkamany, and J. Sabbaghzadeh: *Scr. Mater.*, 2007, vol. 56, pp. 955–8.

[1.30] J. Liu, H. Zhang, and Y. Shi: *Lasers Eng.*, 2012, vol. 23, pp. 265–98.

[1.31] M. Rossini, P.R. Spena, L. Cortese, P. Matteis, and D. Firrao: *Mater. Sci. Eng. A*, 2015, vol. 628, pp. 288–96.

[1.32] G. Cam, S. Erim, C. Yeni, and M. Kocak: *Weld. J. Suppl.*, 1999, pp. 193–201.

[1.33] Q.L. Cui, D. Parkes, D. Westerbaan, S.S. Nayak, Y. Zhou, D.C. Saha, D. Liu, F. Goodwin, S. Bhole, and D.L. Chen: *J. Mater. Eng. Perform.*, 2017, vol. 26, pp. 783–91.

[1.34] E.M. Anawa and A.G. Olabi: *Opt. Laser Technol.*, 2008, vol. 40, pp. 379–88.

[1.35] E.M. Anawa and A.G. Olabi: *J. Mater. Process. Technol.*, 2008, vol. 204, pp. 22–33.

Chapter Two

Experimental Methodology and Manufacturing Background

In order to determine the effects of process parameters on weld properties, an experimental plan was established to produce and analyze samples. Since the samples are based on commercial produced components, context will be provided on the piece and its welded joint (Section 2.1). Following this, the research objectives and sample production procedure will be described (Section 2.2). Then the procedure used to analyze the welded samples will be discussed (Section 2.3). Finally, we will provide an overview of the manufacturing background for each of the mating components welded (Section 2.4).

2.1 Context of Study Application: Planetary Carrier Weld

While the work completed in this thesis will be focused on understanding welds produced between 30MnVS6 and SAE 045 XLF alloys, the specific experimental protocol was adapted to match processing currently implemented for production of a planetary carrier for use within an automatic passenger car transmission. This three-piece welded assembly is comprised of a ring gear, guide disc, and gear spider, and is shown from a side view in Figure 2.1 and as a cross-sectional diagram in Figure 2.2.

Our study will not look at materials currently used in the production of the ring gear and the guide disc; instead, we are focused on understanding a potential new material pairing. For this study we have selected 30MnVS6, a microalloyed ferritic-pearlitic steel alloy, for our ring gear and SAE 045 XLF, a high strength low alloy

(HSLA) steel, for our guide disc. A circumferential butt joint would be present between the 30MnVS6 and SAE 045 XLF alloys. To fabricate this part, the pieces would be rotated so that the laser beam travels along the entire contact interface between the 30MnVS6 and SAE 045 XLF.

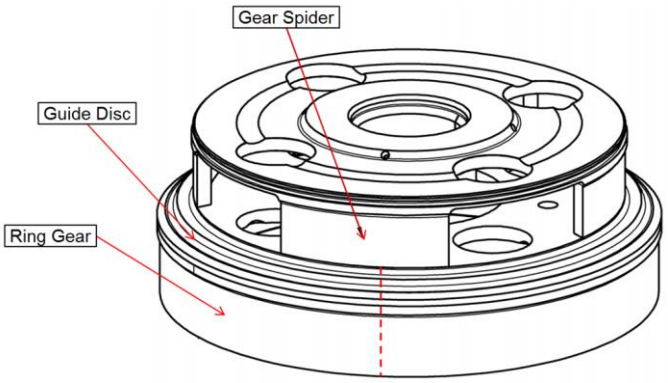

Figure 2.1: A schematic drawing of the assembled planetary carrier. The three sub-components are welded together; however, the focus of this investigation is on the weld between the ring gear and guide disc. The gear spider component will not be discussed in this study.

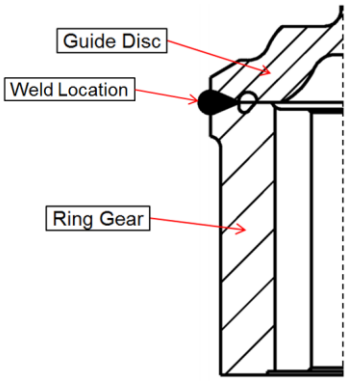

Figure 2.2: Schematic cross-sectional diagram showing the weld location relative to the guide disc and ring gear. This interface to be welded between the two materials is 2.5 mm long. The cross-section location relative to the entire assembly is denoted by the dashed line in Figure 2.1.

2.2 Research Objectives

For the research discussed, there were two objectives for this study of the weld produced between the 30MnVS6/SAE 045 XLF alloys. The first is to establish any relationships between weld parameters (laser power, workpiece speed, and laser beam focal distance) and weld properties. Previous studies have indicated that in other material systems, these parameters have influenced weld geometry, material hardness, microstructural morphology, and weld defect formation. Our second objective of this research was to assess the performance of the manufactured samples under conditions which the welded components might experience as a component within an automotive gearbox. This testing was designed to simulate torsional, cyclic loading.

2.2.1 Laser Welding System Used for Sample Production

Welds between the 30MnVS6 alloy and the SAE 045 XLF alloy were made sequentially using a Trumpf TruDisk 4002 laser welding system. This particular system includes a solid state Nd:YAG laser in a continuous wavelength mode and an inert welding atmosphere was achieved using CO_2 as a shield gas. The laser head remained stationary and the rotation of the workpiece (ring gear/guide disc interface) was accomplished using an integrated Felsomat automation system. This ensured consistent rotation of the samples. Additionally, custom built workpiece fixtures were used which guaranteed the joint location and gap was consistent prior to and during welding. The laser welding setup and parameter ranges are summarized in Table 2.1.

Table 2.1: Description of laser welding system used within this study provided by the manufacturer, Trumpf Inc.

Laser Welding System Properties	
Laser Model	Trumpf TruDisk 4002
Laser Type	Nd:YAG
Power Range	80 – 4,000 W
Wavelength	1.03 μm
Laser Mode	Continuous
Shielding Gas	CO_2
Shielding Gas Flow Rate	10 – 15 L/min
Fiber Optic Cable Diameter	0.2 mm

2.2.2 Selection of Manufacturing Parameters and Methods

Similar to the approach used by Liu [2.1], a full factorial design was applied to the experimental setup allowing for three independent variables to be considered. The three input variables considered included laser power, welding speed, and laser focal position (Table 2.2). Operational parameter ranges were narrowed from system limits by consulting with technical experts experienced in running this particular laser welding setup. These values (Table 2.2) were based on prior experience in welding steel alloys pieces similar to the system used this study. Using the same method as Yoo et al. who concluded that defect-free welds can be produced in S45C steel by limiting the effective heat input from 275 to 435 $J/mm^{0.5} \cdot s^{0.5}$ [2.2], the effective heat input range selected for this trial was between 305 and 325 $J/mm^{0.5} \cdot s^{0.5}$. The complete sample parameter matrix is shown in Table 2.3. In order to negate any external, time-based factors during the production run, the order in which the samples were produced was randomized.

Each of the samples produced was a complete assembly of a ring gear (30MnVS6), guide disc (SAE 045 XLF), and gear spider (proprietary). Two samples were produced for each of the 27 sample types (parameter combinations) outlined in Table 2.3, for a total of 54 samples welded.

Table 2.2: The parameters and adjustment levels used in the full factorial design of experiments. Here laser power, workpiece velocity, and laser focal position were each taken into consideration.

		Factor Levels					
Process Factors	**Symbol**	**Lower**		**Middle**		**Upper**	
		Code	**Actual**	**Code**	**Actual**	**Code**	**Actual**
Laser Power	*P*	-1	1670 W	0	1700 W	1	1730 W
Weld Velocity	*v*	-1	1700 mm/min	0	1750 mm/min	1	1800 mm/min
Focal Position	*f*	-1	-0.05 mm	0	0.00 mm	1	0.05 mm

Table 2.3: Design of experiment plan showing the standardized order used during planning, the randomized run order, and the three parameter variables and levels.

Design of Experiments Parameter Matrix

Standardized Order	Run Order	Laser Power		Weld Speed		Focal Offset	
		P-Code	P-Actual (W)	v-Code	v-Actual (mm/min)	f-Code	f-Actual (mm)
1	17	-1	1670	-1	1700	-1	-0.05
2	10	-1	1670	-1	1700	0	0.00
3	11	-1	1670	-1	1700	1	0.05
4	16	-1	1670	0	1750	-1	-0.05
5	1	-1	1670	0	1750	0	0.00
6	23	-1	1670	0	1750	1	0.05
7	21	-1	1670	1	1800	-1	-0.05
8	8	-1	1670	1	1800	0	0.00
9	3	-1	1670	1	1800	1	0.05
10	12	0	1700	-1	1700	-1	-0.05
11	24	0	1700	-1	1700	0	0.00
12	7	0	1700	-1	1700	1	0.05
13	20	0	1700	0	1750	-1	-0.05
14	25	0	1700	0	1750	0	0.00
15	2	0	1700	0	1750	1	0.05
16	15	0	1700	1	1800	-1	-0.05
17	27	0	1700	1	1800	0	0.00
18	18	0	1700	1	1800	1	0.05
19	5	1	1730	-1	1700	-1	-0.05
20	9	1	1730	-1	1700	0	0.00
21	13	1	1730	-1	1700	1	0.05
22	26	1	1730	0	1750	-1	-0.05
23	4	1	1730	0	1750	0	0.00
24	6	1	1730	0	1750	1	0.05
25	22	1	1730	1	1800	-1	-0.05
26	14	1	1730	1	1800	0	0.00
27	19	1	1730	1	1800	1	0.05

2.3 Experimental Methodology for Characterization of Samples

In order to characterize the welds produced, a series of both non-destructive and destructive tests were performed. A diagram describing the analysis steps and number of samples tested is shown in Figure 2.3. First, visual inspection of all welds was performed in order to assess the presence of surface defects. Following this, ultrasonic inspection of all samples was then performed to determine the presence of sub-surface discontinuities. Destructive testing was then performed on select welded samples produced using the most extreme parameter combinations. These tests included Vickers hardness testing, dimensional measurement, and microstructural characterization of cross-sectioned metallographic samples.

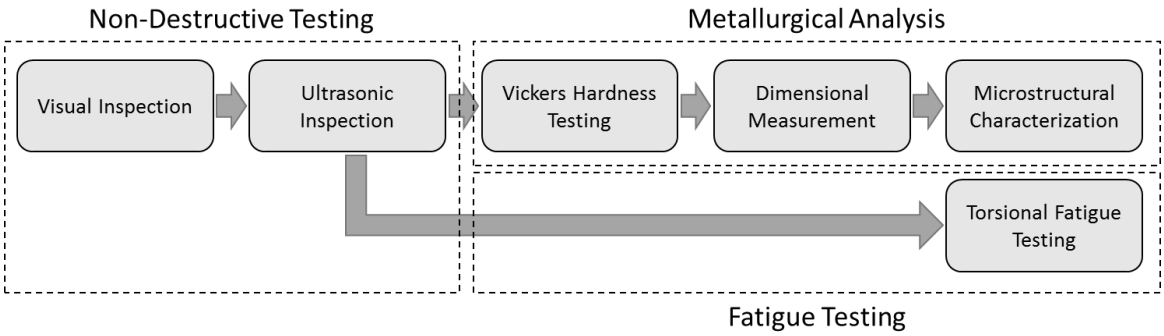

Figure 2.3: Flow chart depicting the steps and selection of samples used for each analysis method.

2.3.1 Visual Inspection of Welded Joints

Visual examination of all samples produced was performed in order to inspect for the presence of defects such voids or cracks open to the welded surface. This inspection was conducted around the entire circumference of the welded components. Additionally, the welded surfaces were inspected for the presence of weld spatter. Images were taken of the start/stop position of each weld. The region of the weld surface exhibiting the most significant amount of weld spatter visible was also photographed as shown in Figure 2.4.

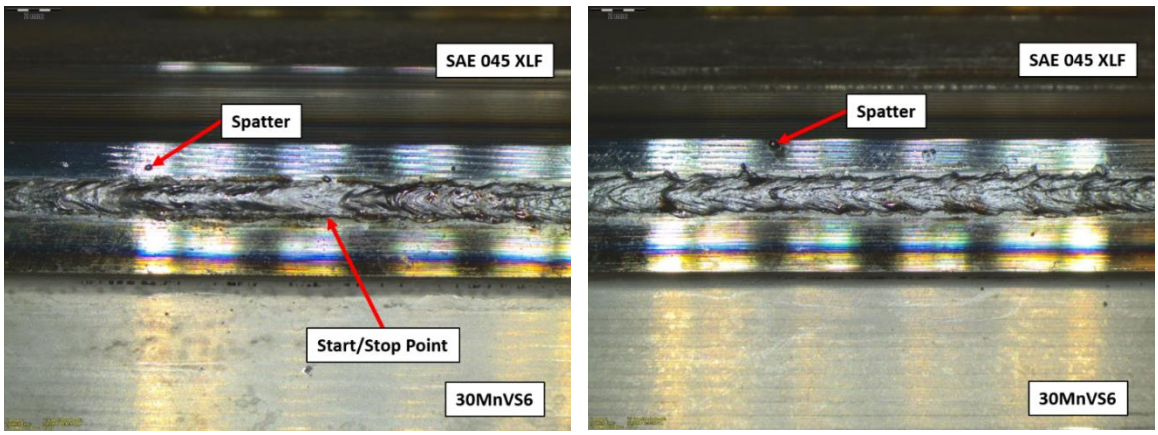

Figure 2.4: Example images taken of the welded surface at the start/stop point of the weld (left) and the area with the most observed spatter present (right). The parameter code of the images shown is 0,0,0.

2.3.2 Subsurface Ultrasonic Inspection of Welds

Prior to destructive testing, ultrasonic non-destructive testing was performed on all samples in order to scan for potential defects or discontinuities. Indications observed during this inspection method were noted as points of interest when performing cross-sectional analysis of the welds.

Ultrasonic inspection involved the generation and transmission of high frequency sound waves through a workpiece. The sound waves were generated by a transducer containing a piezoelectric material which converted electrical signals to mechanical waves. Reflectors such as material interfaces or discontinuities resulted in the reflection of a portion of the soundwave. The reflected soundwave then travels back to the transducer and was then converted back to an electrical signal.

For testing of the welded samples, an immersion ultrasonic system was used. Typically in ultrasonic inspections the transducer is in contact with the workpiece and a couplant is used to assist in the transfer of the soundwave. Couplants are typically a lubricating gel; however, in contrast to a contact ultrasonic setup, immersion inspection involves submerging the workpiece in water. Here, the bath acts as the couplant between the transducer and workpiece. By setting a delay parameter in the ultrasonic system, the sound travel time between the transducer and workpiece was compensated for and allowed for separation between the transducer and workpiece.

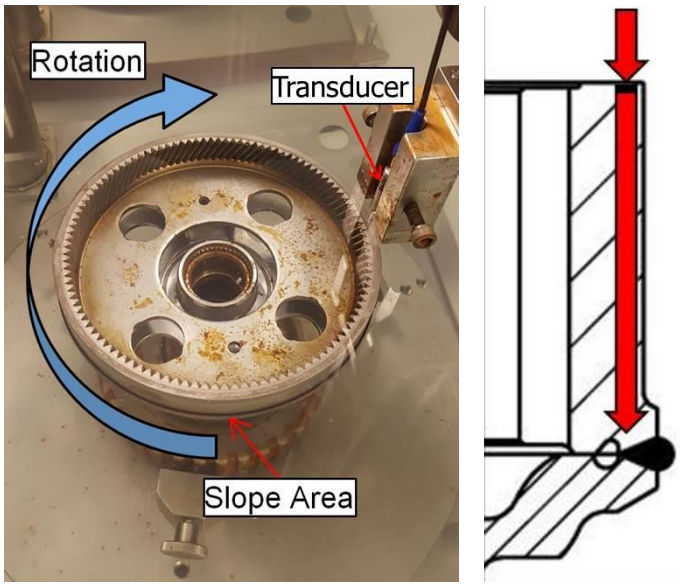

Figure 2.5: Example of a planet carrier sample being scanned via ultrasonic non-destructive testing using an immersion-style system (left). Here, the weld slope, transducer, and rotational direction are shown. Additionally shown (right), is the cross-sectional view of the 30MnVS6 ring gear, SAE 045 XLF guide disc, and weld location as it was mounted in the ultrasonic immersion tank. The sound path is denoted by the red arrows as it travels through the ring gear.

The system used for this application, coupled with an automated 3-axis arm, provides a high level of repeatability as opposed to contact inspection methods which typically require manual movement of the transducer along the workpiece. In addition, the use of a 360º rotational table allows for the scanning of the entire circumference of the part along the welded location. As shown in Figure 2.5, the samples are mounted onto the table by the gear spider, and scanned down through the ring gear.

Data from the ultrasonic inspections was collected in the form of strip charts for each sample. The inspection of the weld was performed through the 30MnVS6 ring gear (Figure 2.5). Here, the weld was 24 mm away from the workpiece surface and was the

focus of the inspection. By setting a "gate" in the ultrasonic inspection system at 24 mm, only the signal amplitude at the weld was taken into consideration. The signal at this location was taken around the entire length of the weld and plotted on a strip chart (Figure 2.6). Based on the shape of the strip chart plot, regions with local amplitude spikes or abnormal patterns could be identified. An example scan of a sample manufactured with an artificial defect is shown in Figure 2.6. Here, a local region of significantly higher amplitude was observed which indicates a greater percentage of the ultrasonic signal is being reflected at this location. Once these areas of interest were identified, metallurgical cross-sections were taken at these locations in order to inspect for weld defects or other discontinuities. By performing ultrasonic testing prior to metallurgical analysis, a greater chance of observing any existing weld defects was possible.

Table 2.4: Ultrasonic parameters used and calculated for the setup used.

Transducer Parameter	Variable/Equation	Value
Frequency	f	5.0 MHz
Diameter	d	6.35 mm
Workpiece Velocity	v	5890 m/s
Near Field	$N = \frac{d^2 f}{4v}$	34.29 mm
Smallest Detectable Flaw	$x = \frac{\lambda}{2} = \frac{v}{2f}$	1.18 mm

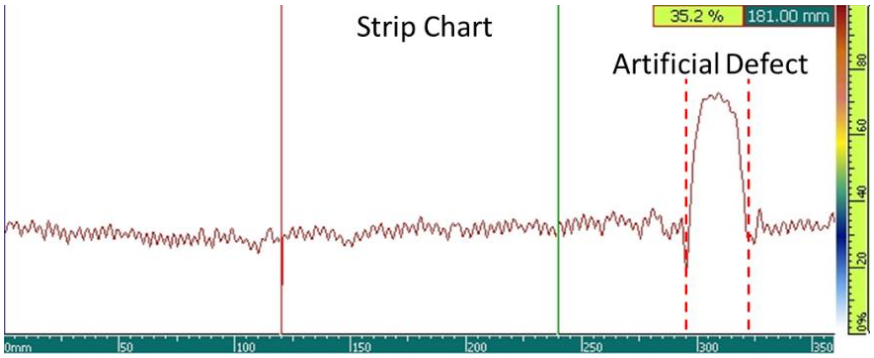

Figure 2.6: Ultrasonic inspection data gathered from a sample manufactured with an artificial defect (i.e. control sample). The strip chart shows the signal amplitude received by the transducer at the weld location around the circumference of the sample.

2.3.3 Preparation of Metallographic Samples

Cross-sections of all samples were cut using an ATM Brilliant 265 metallurgical cut-off saw. These sections were then hot mounted using a Struers CitoPress-1 mounting press and subsequently ground and polished to a 1μm finish using Struers LaboPol-5 polishers according to the grinding and polishing steps described in Table 2.5.

Samples were then tested for hardness across the welds via indentation testing. Following hardness testing, the samples were etched by immersing the sample in 5% nital for 10 s. Nital was selected in order to clearly identify the fusion and heat affected zones of the welded samples [2.3]. Finally, the samples were rinsed with water and immediately dried with pressurized air.

Table 2.5: The grinding and polishing steps used for all mounted metallurgical cross-sections prior to microstructure analysis and hardness testing.

Process	**Grinding 1**	**Grinding 2**	**Grinding 3**	**Polishing 1**	**Polishing 2**
Type	240 grit	800 grit	1200 grit	3 μm Diamond	1 μm Diamond
Pad	SiC Foil	SiC Foil	SiC Foil	Struers MD-Mol	Struers MD-Dac
Lubricant	Water	Water	Water	Struers DP Green	Struers DP Green

2.3.4 Determining Weld Heterogeneity via Hardness Testing

Microhardness testing was performed to understand the evolution of hardness across laser welded joints. Vickers indentation tests were performed across each weld starting and ending within the two parent materials using a Qness Q30A+ testing system. Samples were ground and polished according to the sample preparation procedure described Table 2.5. All samples were tested in the unetched condition in order to prevent the etched surface microstructure from influencing the hardness values. This section outlines both the specific testing parameters along with the anticipated analysis. The testing methods used were based around the ISO 6507-1 standards [2.4].

Vickers hardness testing methodology of welded joints has been well documented within other texts [2.4–12]. The indenter was a pyramid shape where α is the vertex angle of the pyramid-shaped indenter, while δ_1 and δ_2 are the optically measured dimensions of the indentation in the workpiece. The arithmatic mean, δ, between δ_1 and δ_2 was used for the Vickers hardness calculation. As per the ISO 6507-1 standard [2.4], Vickers hardness was determined by the following formula: $Hardness\,(HV) \approx 0.1891\,\frac{F}{\delta^2}$. Additionally, a dwell time of 10 s was used, as specified by ISO 6507-1 [2.4]. The selected separation distance between indents was influenced by both the ISO

standard and academic journals. Initial hardness tests across the weld and base materials using a 0.3 kg load concluded that indentations would be no larger than 0.057 mm; therefore, indentations should be separated by a minimum distance of 0.283 mm in order to keep a seperation distance of five time between each indentation. In order to obtain a more accurate hardness profile across the weld, a staggered pattern was used as shown in Figure 2.7. Here, *d* represents the depth of the welded area, *z* is the spacing between the the two closest indentations, *x* is the resolution between data points across the weld, and *y* is the staggering offset. Y-axis offsets were used in order to increase the distance between neighboring indentations. In order to exceed a minimum separation distance, *z*, of 0.275 mm while achieving a data resolution, *x*, of 0.2 mm, an offset, *y*, of 0.189 mm was required. While a more dense indentation pattern across the weld would hav more spatial resolution, the plastic deformation zones between indentations may overlap skewing the measurement values. Table 2.6 shows the parameters used for hardness profile testing.

Table 2.6: Table listing parameters used during hardness testing across the weld.

Parameter	**Variable**	**Actual Value**
Test Force	*F*	0.3 kg
Indenter Angle	α	136 ^{o}
Dwell Time		10 s
Resolution	*x*	0.20 mm
Indentation Offset	*y*	0.20 mm
Indentation Separation	*z*	0.32 mm
Profile Length		4.00 mm
Number of Indentations		21

The hardness profiles were taken at the midpoint of the weld depth, 1.25 mm below the surface of the base material, as shown by dimension $\frac{d}{2}$ in Figure 2.7. Although the width of the solidification and heat affected zones were only approximately 2 mm at the weld depth midpoint, an additional 1 mm was measured beyond the weld on each side into the base materials. This ensured that the non-heat affected material was sufficiently reached on both sides of the welded area. With a resolution of 0.2 mm achieved across 4.0 mm, a total of 21 indentations were taken per sample.

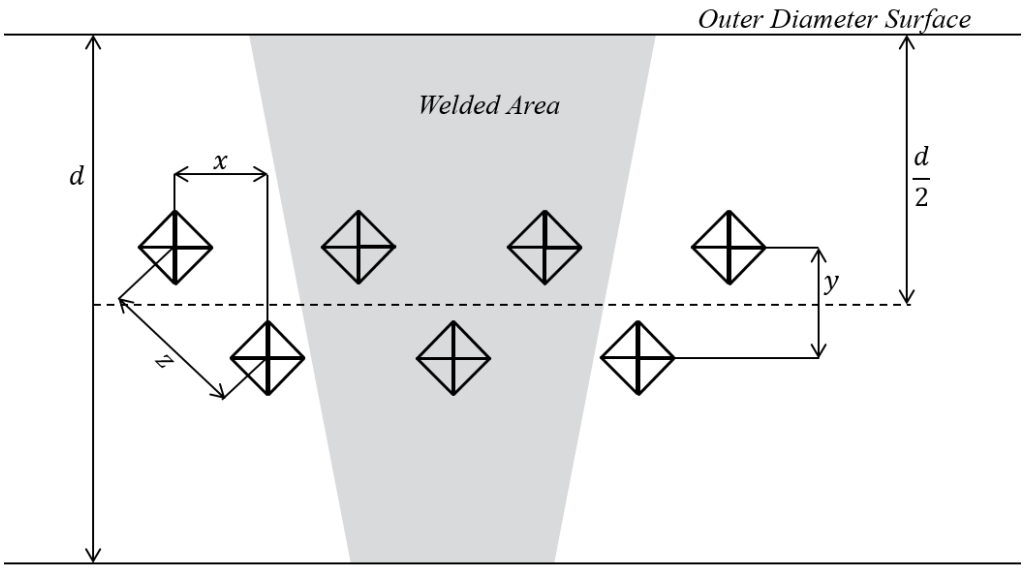

Figure 2.7: Simplified schematic diagram of the weld hardness profile taken relative to the welded area. Here, the weld depth, *d*, spacing between each indentation, *z*, transverse interval distance across the weld, *x*, and longitudinal offset, *y*, is shown.

2.3.5 Dimensional Measurements of Weld Cross-Sections

Dimensional analysis of the sample welds were performed using an Olympus DSX100 digital microscope system. Measurements taken of the heat affected and fusion

zones included depth and width. Referencing the outer diameter of the component, weld depth measurements were taken along the joint centerline. These measurements included both the distance from the outer diameter to the root, and distance from the outer diameter to the lowest point on the weld surface as shown in Figure 2.8. Width measurements of both the solidification and heat affected zones were taken with respect to the weld centerline.

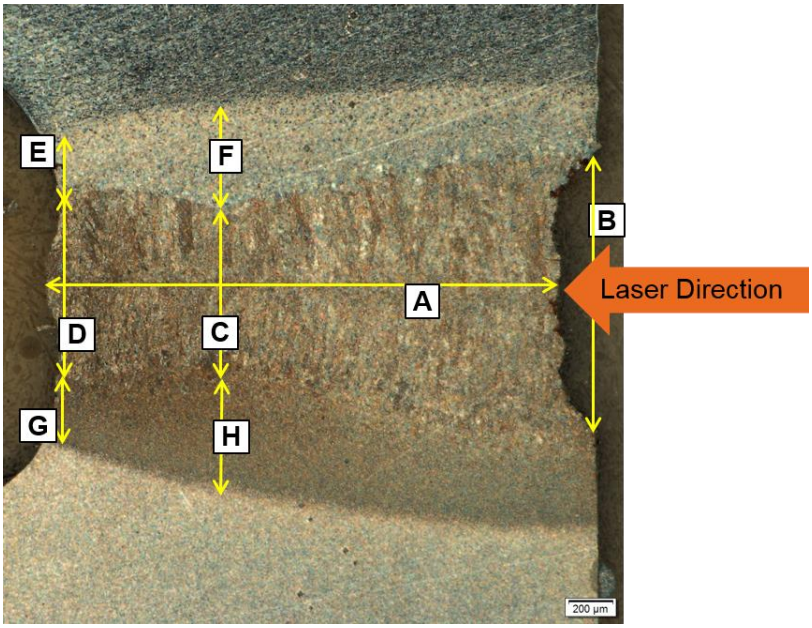

Figure 2.8: A polished and etched weld sample labeled with the various measurements taken throughout the joint.

2.4 Overview of Material Processing Before Laser Welding

30MnVS6 and SAE 045 XLF alloys underwent various manufacturing processes prior the laser welding trials. Figure 2.9, shows a simplified process flow of both the 30MnVS6 ring gear and SAE 045 XLF guide disc from the raw material to laser welding.

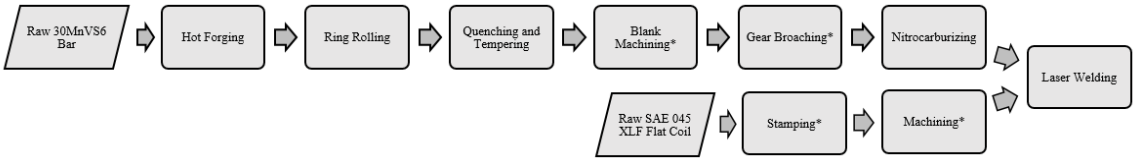

Figure 2.9: Simplified process flow diagram of the studied ring gear (30MnVS6) and guide disc (SAE 045 XLF) components and their primary manufacturing processes. *Processing steps not discussed in this study.

2.4.1 Manufacturing of 30MnVS6 Ring Gears

While this thesis focuses on the interface between the 30MnVS6 and SAE 045 XLF alloys, they were welded as a ring gear and guide disc. This section provides an overview of how the 30MnVS6 alloy was manufactured into a ring gear. Originating from Gerdau Special Steel North America (Gerdau) in the form of 63.5mm round bar stock, the raw 30MnVS underwent deformation-based processing. A ring gear is designed to transfer significant amounts of torque at high speeds from the mating planetary gears; therefore, high strength and a wear resistant surface case are important requirements in its design. For this study, 30MnVS6 material was acquired. This particular grade of steel was produced via electric arc furnace and continuous casting methods achieving a 12.8:1 reduction ratio (Gerdau). Chemical analysis of the heat lot was also supplied (Table 2.7) and met the specifications described in the DIN EN 10267 standard [2.13]. Hardenability data for the received 30MnVS6 batch was also provided by Gerdau in the form of Jominy end quench data performed according to the ASTM A255 standard [2.14]. For the batch of 30MnVS6 tested, the maximum hardness obtainable was 49 HRC (Figure 2.10).

Table 2.7: Chemical composition data of the 30MnVS6 provided by Gerdau according to ASTM A 751 requirements [2.15].

Element	**C**	**Mn**	**P**	**S**	**Si**	**Ni**	**Cr**	**Mo**	**Cu**	**Sn**	**Al**
wt.%	0.27	1.43	0.008	0.034	0.60	0.08	0.15	0.02	0.16	0.007	0.018
Element	**V**	**Nb**	**Ti**	**B**	**Ca**	**N**	**Pb**	**Zn**	**Zr**	**Sb**	
wt.%	0.089	0.002	0.002	0.0005	0.0014	0.0136	0.001	0.003	0.002	0.002	

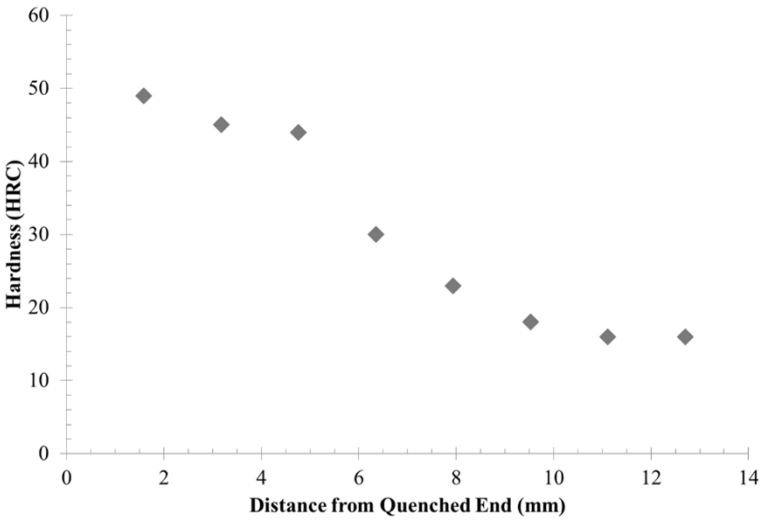

Figure 2.10: Hardenability plot of the 30MnVS6 material used during testing. Here, Jominy end quench testing was performed by Gerdau in accordance with the ASTM A 255-02 standard [2.14].

After characterization of the raw material properties, the 30MnVS6 was cut transversally into cylindrical "slugs" prior to forming operations. Hot forging involved a four step process (1,120 - 1,150 ºC). The first forging impact created the general disc shape of the part, while the subsequent two strikes expanded the width of the cylinder. Finally, the fourth step pierced the center of the disc to form a ring. As the parts exited the forge press, they were immediately transferred to a ring rolling operation (Figure 2.11). The pierced rings gear blanks were passed through the rollers while at elevated

temperatures, which reduced the radial cross-section and refined grain size [2.16]. Following the forming operations, the ring gear blanks were then heat treated. Here the blanks were austenitized at 850 ºC for 150 min, quenched in oil at 65 ºC, and tempered at 650 ºC for 150 min. After heat treatment, the ring gears were then processed to remove the surface scale and adjust the 30MnVS6 ring gears to their final dimensions.

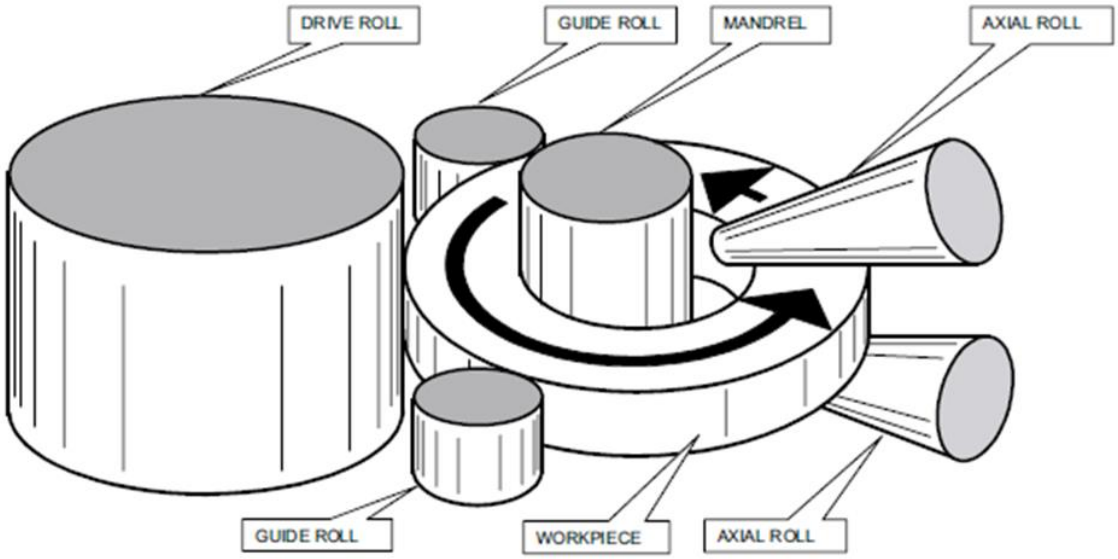

Figure 2.11: Schematic diagram of a typical ring rolling process. Here, the final dimensions of the blank are achieved by the simultaneous rolling of each surface. The axial rollers form the top and bottom surfaces while the drive roll and mandrel form the inner and outer diameters of the blank.

Following the machining and broaching processes, the 30MnVS6 ring gears were processed through a gas nitrocarburizing process. During this process, the material was held at 570 ºC for 60 min in a nitrogen-rich atmosphere. This heat treatment creates a nitride case to form on the surface of the parts which provides significant wear resistance with minimal distortion relative to higher temperature case hardening processes such as

carburizing [2.17]. Following nitrocarburization process, the surface to be laser welded underwent a hard turn machining operation in order to remove the nitrocarburized case.

2.4.2 Production of SAE 045 XLF Guide Discs

This section provides an overview of how the SAE 045 XLF alloy was manufactured into a guide disc. Prior to delivery, these components were stamped from annealed, flat coil stock of SAE 045XLF HSLA steel. The parts were then machined to final dimensions. Table 2.8 lists the chemical composition of the guide discs measured using a SPECTROMAXx optical emission spectroscopy spark tester. The compositional data was as expected according ranges specified by the SAE J 1392 standard [2.18].

Table 2.8: Chemical analysis of the SAE 045XLF guide disc material tested via optical emission spectroscopy and listed according to ASTM A 751 [2.15].

Element	**C**	**Mn**	**P**	**S**	**Si**	**Ni**	**Cr**	**Mo**	**Cu**	**Sn**	**Al**
wt.%	0.06	0.50	0.012	0.005	0.09	0.01	0.04	0.01	0.03	0.008	0.033
Element	**V**	**Nb**	**Ti**	**B**	**Ca**	**N**	**Pb**	**Zn**	**Zr**	**Sb**	
wt.%	0.004	0.035	0.001	0.0002	0.0025	0.001	0.001	0.001	0.003	0.003	

2.4.3 Laser Beam Welding of Planetary Carrier Components

The welding process used to produce the 30MnVS6/SAE 045 XLF planetary carrier was completely automated with the exception of manually programming the parameters for each component according to the experimental design. Induction heating was not used before or after the welding process [2.6]. Once each sample was produced, it was allowed to cool naturally and removed from the production line.

2.5 References

[2.1] J. Liu, H. Zhang, and Y. Shi: *Lasers Eng.*, 2012, vol. 23, pp. 265–98.

[2.2] Y.-T. Yoo, D.-G. Ahn, K.-B. Ro, S.-W. Song, H.-J. Shin, and K. Im: *J. Mater. Sci.*, 2004, vol. 39, pp. 6117–9.

[2.3] G.F. Vander Voort: *Heat Treat. Prog.*, 2001.

[2.4] ISO: in *ISO 6507 - Metallic materials - Vickers hardness test - Part 1: Test method*, vol. 3, 2005, pp. 1–28.

[2.5] G.F. Vander Voort and R. Fowler: *Adv. Mater. Process.*, 2012, vol. 170, pp. 28–33.

[2.6] R.S. Coelho, M. Corpas, J.A. Moreto, A. Jahn, J. Standfuß, A. Kaysser-Pyzalla, and H. Pinto: *Mater. Sci. Eng. A*, 2013, vol. 578, pp. 125–33.

[2.7] M. Rossini, P.R. Spena, L. Cortese, P. Matteis, and D. Firrao: *Mater. Sci. Eng. A*, 2015, vol. 628, pp. 288–96.

[2.8] J.R. Berretta, W. de Rossi, M. David, M. Das Neves, I. Alves De Almeida, N. Dias, and V. Junior: *Opt. Lasers Eng.*, 2007, vol. 45, pp. 960–6.

[2.9] X.N. Wang, Q. Sun, Z. Zheng, and H.S. Di: *Mater. Sci. Eng. A*, 2017, vol. 699, pp. 18–25.

[2.10] C. Xie, S. Yang, H. Liu, Q. Zhang, Y. Cao, and Y. Wang: *J. Mater. Eng. Perform.*, 2017, vol. 26, pp. 3794–801.

[2.11] G. Cam, S. Erim, C. Yeni, and M. Kocak: *Weld. J. Suppl.*, 1999, pp. 193–201.

[2.12] Q.L. Cui, D. Parkes, D. Westerbaan, S.S. Nayak, Y. Zhou, D.C. Saha, D. Liu, F. Goodwin, S. Bhole, and D.L. Chen: *J. Mater. Eng. Perform.*, 2017, vol. 26, pp. 783–91.

[2.13] Normenausschuß Eisen und Stahl: in *DIN EN 10267: Ferritic-Pearlitic Steels for Precipitation Hardening From Hot-Working Temperatures*, 1998, pp. 1–18.

[2.14] ASTM International: in *ASTM A 255 - 02: Standard Test Methods for Determining Hardenability of Steel*, vol. 2, 2002, pp. 1–24.

[2.15] ASTM International: in *ASTM A 751 - 01: Standard Test Methods , Practices , and Terminology for Chemical Analysis of Steel Products*, vol. 3, 2001, pp. 1–5.

[2.16] J. Guo, D. Qian, and J. Deng: *J. Mater. Process. Technol.*, 2016, vol. 231, pp. 151–61.

[2.17] L. Epler: *Gear Technol.*, 2000, pp. 24-25.

[2.18] SAE International: in *SAE J 1392: Steel, High Strength, Hot Rolled Sheet and Strip, Cold Rolled Sheet, and Coated Sheet*, SAE International, 2008, pp. 1–10.

Chapter Three

Characterization of Microstructural Changes After Laser Welding

Analysis of the welded samples and interpretation of the data acquired was completed in order to determine the influence of the varied parameters on the welds produced. The sampling selection of the laser welded 30MnVS6 and SAE 045 XLF alloys is presented (Section 3.1). Hardness testing of the sampled components is then described (Section 3.2), followed by dimensional measurements (Section 3.3), and observed microstructures (Section 3.4). We then summarize discuss the findings (Section 3.5). Discussion of torsional fatigue testing will be presented in Chapter 4.

3.1 Sampling Selection for Metallurgical Testing

In order to most effectively observe reactions in weld properties (i.e. hardness, geometry, microstructure, defects) testing was broken up into two segments, Phase I and II. The samples selected for Phase I metallurgical testing were those produced using the most extreme parameter combinations (Table 3.1).

Aside from the nominal 0,0,0 sample, all other samples tested were from the extremes of the parameter ranges. Since these were the most extreme parameter combinations, any variations in weld properties would likely be most significant in these parts. Additionally, there would be a greater chance in observing the presence of defects in these particular samples. The remaining samples were reserved for Phase II of testing.

Table 3.1: Phase I samples selected for hardness, dimensional, and microstructural analysis.

Standardized Order	Run Order	Laser Power		Weld Speed		Focal Position	
		P-Code	P-Actual (W)	v-Code	v-Actual (mm/min)	f-Code	f-Actual (mm)
1	17	-1	1670	-1	1700	-1	-0.05
3	11	-1	1670	-1	1700	1	0.05
7	21	-1	1670	1	1800	-1	-0.05
9	3	-1	1670	1	1800	1	0.05
14	25	0	1700	0	1750	0	0.00
19	5	1	1730	-1	1700	-1	-0.05
21	13	1	1730	-1	1700	1	0.05
25	22	1	1730	1	1800	-1	-0.05
27	19	1	1730	1	1800	1	0.05

3.2 Weld Heterogeneity via Indentation Testing

Results of the hardness profile in the form of a boxplot can be seen in Figure 3.1. Here, it can be seen that the highest hardness region was 0.6 to 0.8 mm into the 30MnVS6 material and hardness values leveled off at 1.2 mm beyond either side of the weld centerline. Furthermore, variation in hardness values on the SAE 045 XLF side of the weld can be observed at 0.4 mm from the weld centerline. Hardness of the SAE 045 XLF base material 2.0 mm from the weld centerline was 169.3 HV0.3 with a standard deviation of 4.31 HV0.3, while the base 30MnVS6 material at 2.0 mm from the weld centerline was 255.3 HV0.3 with a standard deviation of 8.86 HV0.3. Measurement outliers were only observed between -1.0 and 1.0 mm from the weld centerline suggesting that the hardness of the base materials was more consistent relative to the fusion and heat affected zones. Microstructural non-uniformity, specifically in the heat affected zones where the microstructure exhibited a gradual transition across the region.

Potential causes for outliers not present near weld zone interfaces, such as the outlier present at 0.0 mm, could be due to the presence of a local microstructural discontinuity.

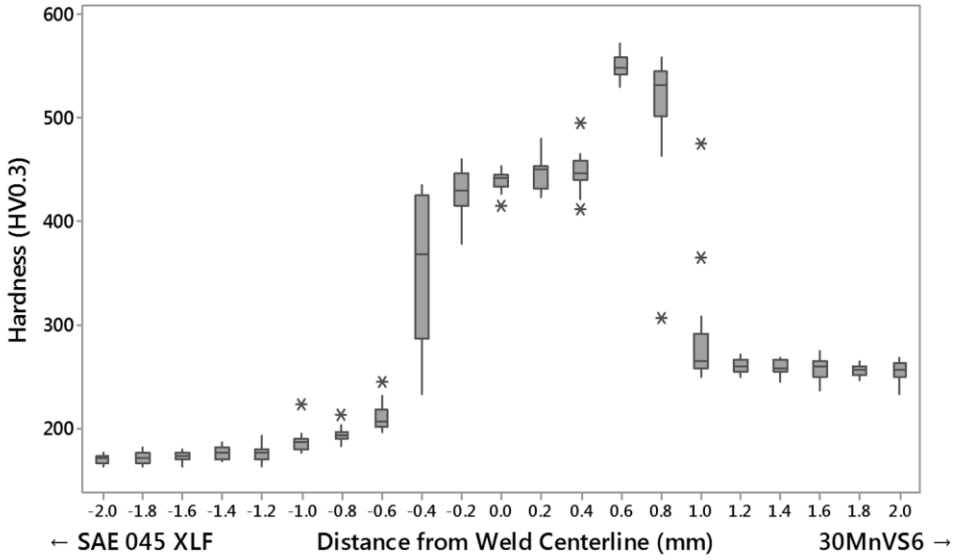

Figure 3.1: Boxplot showing the hardness profile taken from two locations in each of the nine analyzed weld samples.

3.3 Dimensional Measurement of Weld Cross-Sections

Various measurements were taken throughout the weld cross-section which were described in Chapter 2, Section 2.3.5. Measurements of the solidification zone were taken at the root, surface, and the narrowest point. Additionally, the effective weld depth was measured. In the heat affected zones, the widest and most narrow points were recorded. Data collected from the cross-sectional measurements can be in Table 3.2. No significant sources of variation were observed across any of the analyzed samples.

Table 3.2: Table showing the various weld dimensions taken from two locations in each of the nine analyzed weld samples.

Measurement	Measurement Description	Average (mm)	Std. Dev. (mm)
A	Effective Weld Depth	2.468	0.073
B	Solidification Zone Width (Surface)	1.259	0.082
C	Solidification Zone Width (Min.)	0.730	0.050
D	Solidification Zone Width (Root)	0.868	0.080
E	SAE 045 XLF Minimum HAZ Width	0.642	0.029
F	SAE 045 XLF Maximum HAZ Width	0.921	0.063
G	30MnVS6 Minimum HAZ Width	0.736	0.033
H	30MnVS6 Maximum HAZ Width	0.983	0.055

3.4 Characterization of Weld Microstructure

Optical microscopy and microstructural characterization of the joints was completed using an Olympus BX51M upright metallurgical microscope. An overview of the welded cross-section is shown in Figure 3.2, which exhibited five distinct regions. Regions A and E represent the SAE 045 XLF and 30MnVS6 base materials, respectively. Location C denotes the fusion zone where material was melted and re-solidified during the welding process. The intermediate regions of B and D are the heat affected zones which exhibit microstructural transitions from the base material to the welded material due to the varying degrees of exposure to thermal energy produced by the welding operation.

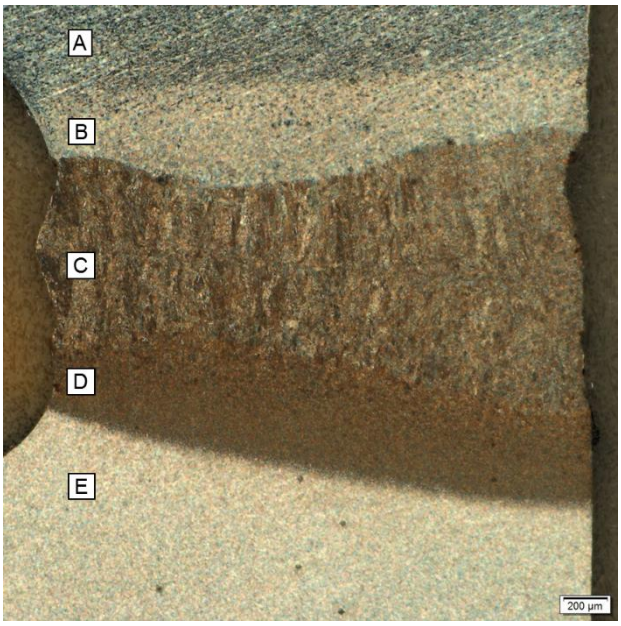

Figure 3.2: Cross-section of weld from the parameter middle point sample (0, 0, 0). The sample was etched using 5% nital. Here, the five distinct microstructural regions were observed as the (A) SAE 045 XLF base material, (B) SAE 045 XLF heat affected zone, (C) solidification zone, (D) 30MnVS6 heat affected zone, and (E) 30MnVS6 base material.

The base SAE 045 XLF structure appeared consistent with having been supplied and welded in a cold-rolled and annealed condition. Equiaxed ferritic grains were present along with a distribution of precipitated carbides are apparent in Figure 3.3. Alternatively, the base 30MnVS6 microstructure was a much finer mix of ferrite and pearlite. This structure was consistent with the hot forged, quenched and tempered, and nitrocarburized condition it was received and welded in.

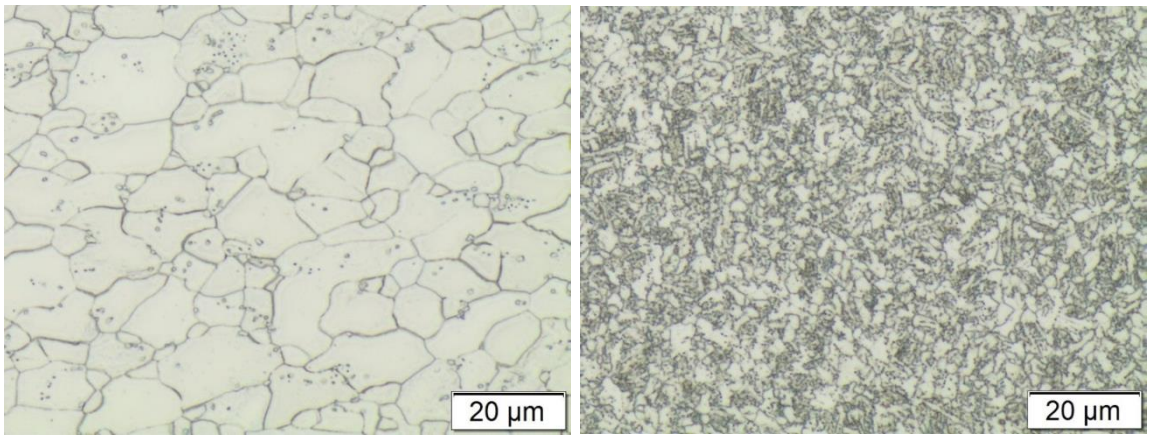

Figure 3.3: Microstructures of the base SAE 045 XLF (left) and 30MnVS6 (right).

In the SAE 045 XLF heat affected zone, the primary microstructural constituent was ferrite; however, in this region increasing degrees of recrystallization and grain coarsening was observed approaching the solidification zone. Closest to the unaffected base material, recrystallization was observed nucleating from triple points, grain boundaries, and intracrystalline discontinuities (i.e. inclusions, precipitates, carbides) (Figure 3.4). Since a less thermal energy from the laser welding process was present at the transition between the SAE 045 XLF base material and heat affected zone, energy for growth of the recrystallization was limited. Towards the center of the SAE 045 XLF heat affected zone, the amount of thermal exposure was more extreme and growth of the recrystallized phase was increasingly evident as seen in Figure 3.4. The nucleation in this region is believed to be a secondary ferritic phase.

Closer to the weld, Figure 3.5 exhibits the transitional region between the SAE 045 XLF heat affected zone and solidification zones. Here, an increasing amount of Widmanstätten ferrite can be observed within the grain structure as a result of the

significantly elevated temperature achieved during welding. This variant of the base ferritic phase is formed at temperatures near the A_3 temperature of high strength low alloy steels [3.1]; however, contrary to the formation of martensite where the material is rapidly cooled from above its A_3 temperature, the amount of undercooling is not substantial enough for martensitic plate to form and relieve strain [3.1]. Hardness values in this region, represented by the data taken 0.6 mm into the SAE 045 XLF material from the weld centerline, was averaged at 210.6 HV0.3 with a standard deviation of 13.1 HV0.3.

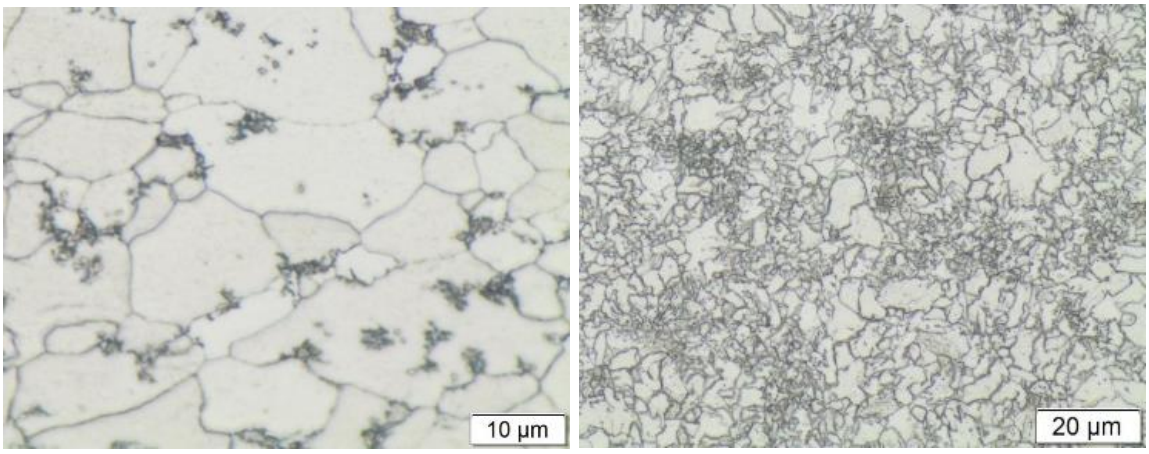

Figure 3.4: Microstructural transition across the SAE 045 XLF heat affected zone. Closest to the base material, secondary phase nucleation can be observed (left), while closer to the fusion zone the presence of the precipitating phase is more extensive (right).

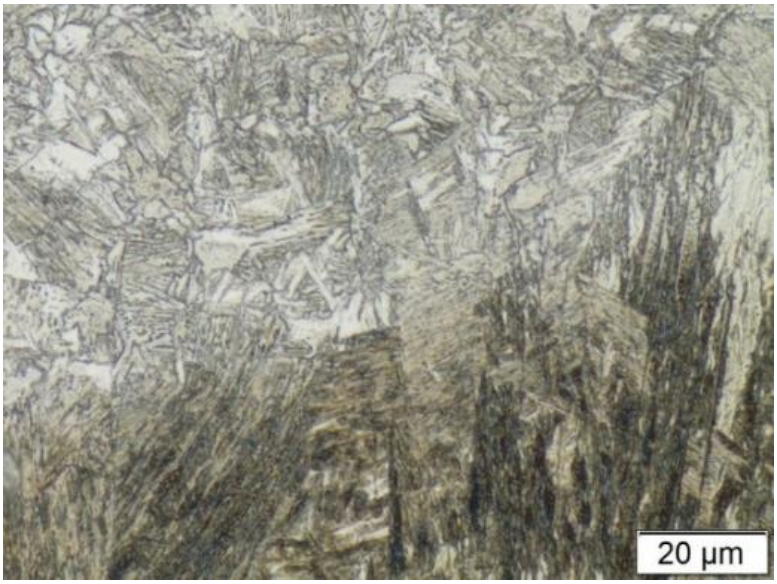

Figure 3.5: At the interface between the SAE 045 XLF heat affected and solidification zones, the formation of Widmanstätten ferrite was observed.

The solidification zone microstructure was consistent through each location (two locations per each of the sample types) with regards to structure and observed martensitic packet size. Shown in Figure 3.6, lath martensite was the primary constituent of the microstructure. An average of hardness values at the centerline (0.0 mm) was 439.0 HV0.3 across all nine samples tested with a standard deviation of 9.6 HV0.3. This average hardness value was less than that of the 30MnVS6 Jominy hardenability test which achieved 49 HRC, or approximately 500 HV10 when converted using ISO 18265 Table A.1. Considering standard Jominy end quench testing conditions involve a relatively more aggressive water quench than air cooling after welding, the slightly lower hardness values obtained are expected. Based on observations, this region also had the largest martensitic packet size throughout the joint or in either of the base materials.

With a larger martensitic packet size, a Hall-Petch relationship may have also contributed to the slightly lower than expected hardness in this zone [3.2].

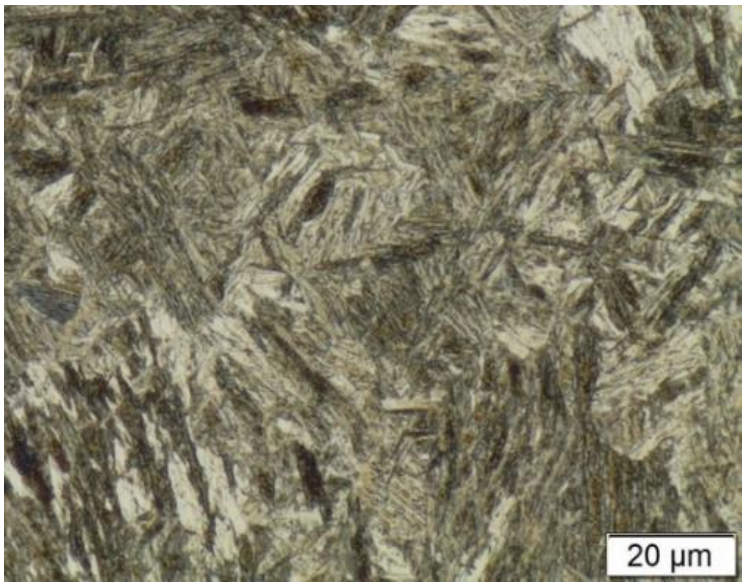

Figure 3.6: Lath martensite present throughout the weld solidification zone.

In between the solidification zone and the 30MnVS6 base material, a region of progressive grain coarsening was observed. Bordering the base material, the grain size of the heat affected zone appeared to be the same size as the base material, and coarsened until it matched the size of the solidification zone grain size. The average hardness observed at 0.6 mm across all sampled location was 550.3 HV0.3 with a standard deviation of 11.8 HV0.3, the hardest of all zones throughout the weld. As per ISO 18265 Table A.1, the obtained value of 550.3 HV0.3 converted to approximately 52.3 HRC, which was over 3 HRC higher than the highest value obtained during Jominy end quench testing.

Microstructurally, the phase present was similar to that of the solidification zone but with a finer martensitic packet size. Like that of the SAE 045 XLF heat affected zone, the grain structure appeared to be the same size as that of the 30MnVS6 base material and coarsened throughout the heat affected zone, eventually matching that of the solidification zone.

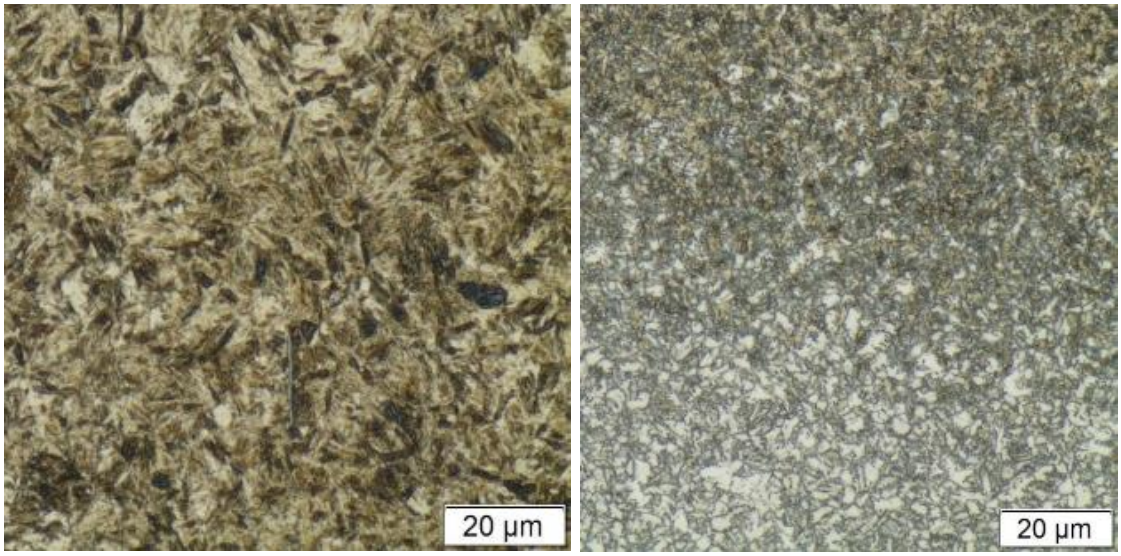

Figure 3.7: Primary heat affected microstructure of the 30MnVS6 material (left) and the heat affected zone's transition with the base 30MnVS6 material (right).

3.5 Discussion

Additional analysis and insight will be provided on various aspects of this study. First we will assess the influence of welding parameters (i.e. power, speed, focal position) on the properties (i.e. hardness, microstructure, geometry) of the 30MnVS6/SAE 045 XLF joints produced (Section 3.5.1). Finally, the achievement of having manufactured joints involving a material containing a high carbon equivalent will be described (Section 3.5.2).

3.5.1 Influence of Parameters on Weld Properties

When considering each of the five distinct regions of each weld produced (i.e. heat affected zones, solidification zone, and base materials), very little variation was seen across the components tested (Table 3.3). This suggests that the welding parameters selected had minimal impact on the intrinsic morphology and properties of each region.

Table 3.3: Average hardness for weld regions. The data shown was collected at two locations for each of the nine samples examined in Phase I.

Weld Region	Distance from weld centerline (mm)	Hardness (HV0.3) Average ± St. Dev.
Guide Disc BM	-2.0	169.3 ± 4.3
Guide Disc HAZ	-0.6	210.6 ± 13.1
Solidification Zone	0.0	439.0 ± 9.6
Ring Gear HAZ	0.6	550.3 ± 11.8
Ring Gear BM	2.0	255.3 ± 8.9

As discussed in Chapter 1, various fundamental weld characteristics can be related to the relationship between workpiece velocity and laser power. In some cases, defects (i.e. porosity and spatter) can be formed if this ratio becomes too extreme due to changes in the weld pool shape. By examining samples of varying power to workpiece velocity levels the overall size of the welded joints were not significantly impacted. As previous research has shown, weld penetration depth is most significantly influenced by the balance of laser power and workpiece velocity [3.3–7]. This may have been more evident on a thicker workpiece as the parameters selected were sufficient enough to penetrate the entirety of the sample.

3.5.2 Welding Without Preheating

Despite a lack of significant response to variation in welding parameters, the fact that robust laser welded joints were able to be consistently produced without the assistance of an induction heating process was beneficial. Preheating and postheating operations are often recommended for the welding of steel alloys with carbon equivalents over 0.35 due to excessive hardenability and susceptibility to hydrogen cracking [3.8]. As discussed in Section 1.2.3, the 30MnVS6 alloy used for welding has a carbon equivalent of 0.60 making it a traditionally recommended candidate for a pre- or postheating process.

The benefits of induction pre- and postheating have been discussed by Coelho et al. for the use of laser welding of S500MC high strength low alloy steel [3.9]; however, the avoidance of this type of processing can save money in terms of both capital investment and operating costs (i.e. electricity, maintenance). Additionally, by being able to successfully manufacture planetary carriers without induction preheating, a significant reduction in product variation can be achieved.

During production, the use of induction preheating not only heats the components to be welded, but inadvertently imparts thermal energy into the workpiece fixturing as well. This heat buildup leads to thermal expansion of the workpiece fixtures and results in variation of the joint location relative to the fixed laser position. Alone, the thermal expansion of the workpiece carrier can result in a positional deviation of the joint, but furthermore the fit between the workpiece and fixture can be affected further exasperating any variation. Without a proper fit between the workpiece and fixture,

severe misalignments can occur resulting in machine damage and fabrication of nonconforming product.

Ideally, a constant or predictable thermal expansion could be compensated for with a variable positioned laser; however many unpredictable factors must be considered. Short, intermittent machine stoppages such as equipment faults in addition to longer, planned downtimes such as can allow the fixturing to cool and reheat. With these interruptions to consider, predicting the thermal expansion of fixturing becomes a more complex issue. Positional sensors and other devices are available which could provide the ability to track the joint location; however, this adds another layer of complexity to the machinery. In industry the reduction of machine downtime is critical; therefore, process simplicity is ideal.

In extreme cases where the offset between the joint and the laser position becomes too great, incomplete fusion of the weld joint can occur and result in premature failure of the weld in service. One such example where excessive positional variation between the joint and laser fixture resulted in the premature failure of a similar planetary carrier in service is shown in Figure 3.8. Here, the offset of the weld centerline is measured relative to the original interface between the two joined components and an offset of over 400 μm was observed. Failure originated at the portion of the joint that was not effectively joined and propagated between the guide disc's heat affected zone and base material.

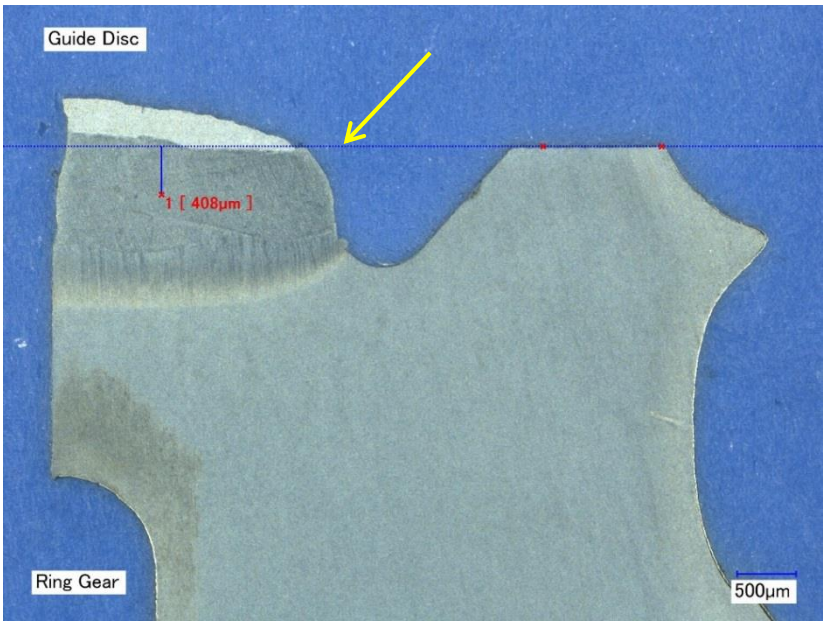

Figure 3.8: A cross-section of a failed planetary carrier caused by an offset between joint location and laser position. Here, the fracture occurred between the guide disc base material and heat affected zone resulting in premature failure of the weld during service. The origin of the failure is denoted by the arrow.

By concluding that the 30MnVS6 alloy could be effectively laser welded without the assistance of an induction preheating process, the planetary carrier manufacturing process can be significantly simplified. This conclusion further suggests that careful material selection plays a critical role in industry and is often beneficial to both production quality and cost.

3.6 References

[3.1] H. Bhadeshia and R. Honeycombe: in *Steels: Microstructure and Properties*, 4th edn., Elsevier Ltd., 2017, pp. 69–78.

[3.2] B.L. Bramfitt and B.S. Corporation: *Met. Handb. Desk Ed. Second Ed.*, 1998, pp. 153–73.

[3.3] Y.-T. Yoo, D.-G. Ahn, K.-B. Ro, S.-W. Song, H.-J. Shin, and K. Im: *J. Mater. Sci.*, 2004, vol. 39, pp. 6117–9.

[3.4] A.P. Tadamalle, Y.P. Reddy, and E. Ramjee: *Adv. Prod. Eng. Manag.*, 2013, vol. 8, pp. 52–60.

[3.5] A.P. Tadamalle, Y.P. Reddy, E. Ramjee, and V.K. Reddy: *Adv. Prod. Eng. Manag.*, 2014, vol. 9, pp. 128–38.

[3.6] F. Malek Ghaini, M.J. Hamedi, M.J. Torkamany, and J. Sabbaghzadeh: *Scr. Mater.*, 2007, vol. 56, pp. 955–8.

[3.7] S. Katayama: in *Handbook of Laser Welding Technologies*, Woodhead Publishing Limited, 2013, pp. 3–15, 47–72.

[3.8] D.L. Olson, ed.: in *ASM Handbook: Welding, Brazing, and Soldering*, vol. 6, ASM Intl, 1993, pp. 229–48, 756–76, 1083–5.

[3.9] R.S. Coelho, M. Corpas, J.A. Moreto, A. Jahn, J. Standfuß, A. Kaysser-Pyzalla, and H. Pinto: *Mater. Sci. Eng. A*, 2013, vol. 578, pp. 125–33.

Chapter Four

Assessment of Weld Fatigue Performance

Fatigue testing can be used to predict the durability of a component that will undergo cyclic loading. For laser welds between both similar and dissimilar alloys, this technique can help determine the durability of a welded joint and has been used extensively (Table 4.1) [4.1–7]. For this study, torsional fatigue testing of the 30MnVS6/SAE 045 XLF joints was to simulate expected service conditions within an automotive gearbox with regards to loads and cycles. Based on the results of this testing, it could be concluded whether or not this dissimilar alloy joint could be implemented in real-world applications. In this chapter, we will first review the experimental setup (Section 4.1). Then, we will discuss the results obtained (Section 4.2) and finally their significance to this research (Section 4.3).

Table 4.1: Fatigue studies performed on similar and dissimilar laser welding systems.

Primary Author	**Material A**	**Material B**	**Citation**
Cao, L.	AISI 316L	EH36	[4.1]
Xie, C.	DP590	n/a	[4.2]
Sonsino, C.	S355N S355M S690Q S960Q	n/a n/a n/a n/a	[4.3]
Wang, X.	DP780	n/a	[4.4]
Cui, Q.	DP980	HSLA	[4.5]
Zengliang, G.	16MnR	n/a	[4.6]
Cam, G.	AISI 316	St37	[4.7]

4.1 Experimental Method

Fabrication of samples was previously described in Chapter 2, Sections 2.2 and 2.4. Based on our results summarized in Chapter 3, Sections 3.2-4, minimal variation in fatigue performance should be observed based on the lack microstructure and hardness variations observed in the samples analyzed. Additionally, the lack of structural weld defects (i.e. voids, cracking) present in the samples suggest that there are limited sites suitable for fracture initiation.

4.1.1 Sample Selection for Fatigue Testing

Samples were modified with a mounting plate which allowed for the fixture to apply a load directly to the ring gear. Typically in service, the ring gear is loaded on its gear teeth by mating gear. By attaching the mounting plate directly to the base of the 30MnVS6 ring gear (Figure 4.1), the load path was able to bypass the gear teeth and be transferred directly to the weld. The other side of each sample was anchored by four fixed pins which passed through the SAE 045 XLF guide disc.

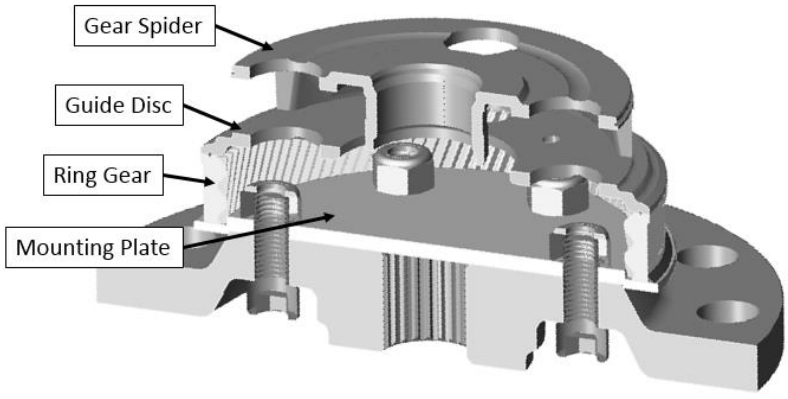

Figure 4.1: Fixturing setup for fatigue testing of the welded samples. The gear spider was not present during fatigue testing.

4.1.2 Testing Parameters and Equipment Setup

Torsional fatigue testing was performed at room temperature using an Instron servo-hydraulic torsional fatigue system as shown in Figure 4.2. Testing parameters used for the experiment are listed in Table 4.2. During testing, the samples were loaded unidirectionally between 30 and 3,500 N·m at a frequency of 13 Hz. These selected testing parameters were recommended by applications testing experts based on the durability limits of similar planetary carriers. It was believed that this loading configuration would result in component failure if any significant defects were present. In order to monitor for sample failure in the form of crack propagation or plastic deformation, the angular deflection of each sample was continuously monitored throughout testing. If the angular deflection of the component exceeded a designated limit of 0.07°, the system was programmed to automatically shut down in order to prevent damage to the test equipment. The fatigue testing was programmed to run without interruption for a maximum of 2,000,000 cycles.

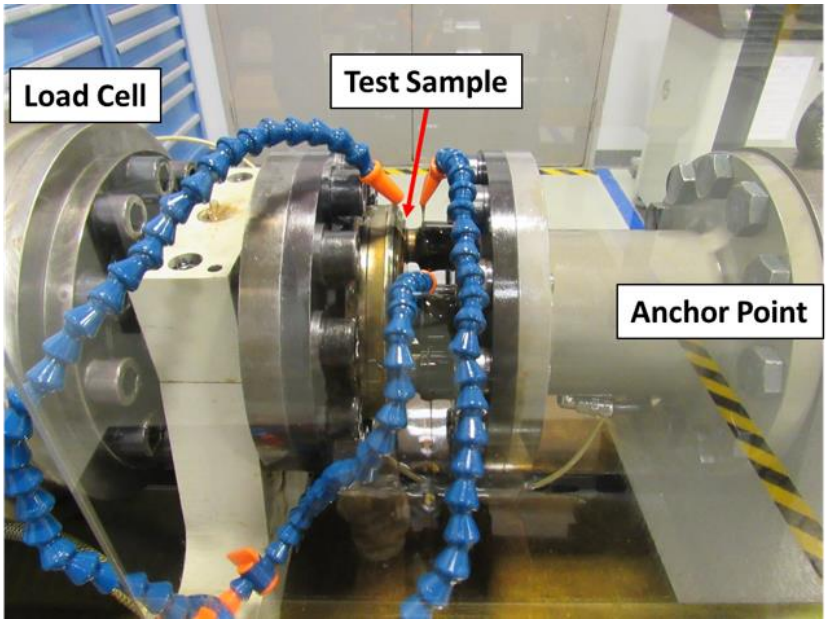

Figure 4.2: Fatigue testing system used to cyclicly load the welded components in order to simulate loading conditions during service.

Table 4.2: Parameters used for torsional fatigue testing of the welded planetary carrier samples.

Parameter	**Value**	
Loading Configuration	Torsional Unidirectional	
Main Load	3,500	N·m
Preload	30	N·m
Frequency	13	Hz
Maximum Cycles	2,000,000	cycles

4.2 Results of Torsional Fatigue Testing

No sample fractured or exceeded 0.07° deflection, and therefore all samples ran continuously through the two million cycle testing program. Results are shown in Table 4.3. Once the cycles were completed, the parts were removed from the test fixture and visually inspected. There were no defects or damaged areas observed.

Table 4.3: Torsional fatigue testing results. No failures were observed for any samples tested through two million cycles.

Standardized Order	Laser Power (W)	Weld Speed (mm/min)	Focal Position (µm)	Power to Speed Ratio	Cycles Performed	Failure Location
7	1670	1800	-5.0	0.928	2,000,000	No Failure
9	1670	1800	5.0	0.928	2,000,000	No Failure
14	1700	1750	0.0	0.971	2,000,000	No Failure
19	1730	1700	-5.0	1.018	2,000,000	No Failure
21	1730	1700	5.0	1.018	2,000,000	No Failure

4.3 Discussion

Torsional fatigue testing using loads up to 3,500 N·m for two million cycles did not cause failure in any of the 30MnVS6/SAE 045 XLF welds. The consistency of these results was aligned with the lack of variation in weld geometry and hardness between samples produced using varying laser power, workpiece speed, and focal position parameters. Additionally, the lack of structural defects (i.e. cracks, voids) observed in the weld microstructure is in line with not having observed any premature failures during fatigue testing. This testing has established that even with the introduction of process parameter variations, welded joints can be effectively produced between 30MnVS6 and SAE 045 XLF alloys. This information is important for the potential implementation of these joints in commercial gearbox applications.

4.4 References

[4.1] L. Cao, X. Shao, P. Jiang, Q. Zhou, Y. Rong, S. Geng, and G. Mi: *Metals (Basel).*, 2017, vol. 7, pp. 1–13.

[4.2] C. Xie, S. Yang, H. Liu, Q. Zhang, Y. Cao, and Y. Wang: *J. Mater. Eng. Perform.*, 2017, vol. 26, pp. 3794–801.

[4.3] C.M. Sonsino: *Int. J. Fatigue*, 2009, vol. 31, pp. 88–101.

[4.4] X.N. Wang, Q. Sun, Z. Zheng, and H.S. Di: *Mater. Sci. Eng. A*, 2017, vol. 699, pp. 18–25.

[4.5] Q.L. Cui, D. Parkes, D. Westerbaan, S.S. Nayak, Y. Zhou, D.C. Saha, D. Liu, F. Goodwin, S. Bhole, and D.L. Chen: *J. Mater. Eng. Perform.*, 2017, vol. 26, pp. 783–91.

[4.6] G. Zengliang and Z. Kangda: *J. Mater. Process. Technol.*, 1997, vol. 63, pp. 559–62.

[4.7] G. Cam, S. Erim, C. Yeni, and M. Kocak: *Weld. J. Suppl.*, 1999, pp. 193–201.

Chapter Five

Conclusions and Suggested Future Research Directions

This study investigated the microstructural evolution and fatigue performance of laser welded joints between dissimilar steel alloys, 30MnVS6 and SAE 045 XLF. These were selected due to their relevance to the automatic gearbox manufacturing industry. Welding parameters including laser power (1,670 – 1,730 W), workpiece speed (1,700 – 1,800 mm/min), and focal position (-0.05 – 0.05 mm) were varied in order to determine their influence on the welds produced. This chapter first summarizes the relationships between the varied process parameters, microstructure, and properties of the 30MnVS6/SAE 045 XLF welds (Section 5.1). Following this, a discussion is provided with regards to weld preheating and how this technique was not needed for the 30MnVS6 alloy (Section 5.2). The next section discusses the conditions that were met in order to produce welds free of cracks or voids (Section 5.3). The following section highlights the performance of the welded samples following torsional fatigue testing (Section 5.4). Finally, we will provide insight into potential opportunities for future research studies (Section 5.5).

5.1 Parameter Influence on Microstructure and Hardness

Microstructural analysis of samples exhibited three distinct phases shared between each part in addition to the two base microstructures. Analysis of the microstructures showed that all welds contained a coarse morphology of lath martensite within the fusion zones. On the side of the ferritic SAE 045 XLF alloy, the heat affected zone exhibited nucleation of a second phase at the grain boundaries of the base ferrite phase. Closer to

the fusion zone in this material, the distribution of this nucleating phase increased and the presence of Widmanstätten ferrite was more prevalent. On the 30MnVS6 alloy side, a fine ferrite-pearlite microstructure transitioned to lath martensite whose packet size increasingly coarsened until matching that of the fusion zone. Quantification of material grain size was not performed since the differences observed between each of the microstructural zones were significant enough to qualitatively categorize. Additionally when approaching the fusion zone, grain size coarsened throughout both of the heat affected zones making this attribute difficult to enumerate.

Prior research indicated that variation of both laser power and workpiece speed should have produced the greatest response with regards to weld penetration depth [5.1–5]. In designing this study, we relied on both the instrumentation limitation and input from technical experts to select the parameter ranges for the laser power, work piece speed, and focal point adjustments. Still, the parameter ranges selected to manufacture the welds were not diverse enough to significantly alter the microstructure between the nine sample types. Despite the laser system's ability to reach 4,000 W, a relatively narrow power range (1,670 to 1,730 W) was selected based on the thickness of the samples to be welded. The selection of a relatively thin workpiece is likely to have negated any observable variation of weld depth as the parameter ranges selected were powerful enough to generate welds completely through the samples. A thicker workpiece (greater than 5.0 mm) would likely have been more susceptible to influence of welding parameters on weld depth.

5.2 Assessment of Preheating Requirements

It was discussed in Chapter 1, Section 1.2.3, that preheating and postheating is used to reduce the susceptibility of cold cracking and excessive hardening of metals. Assessment of the carbon equivalent for ferrous alloys has been used as a guideline for determining this requirement. However, it has been shown that there are numerous variations of carbon equivalent formulae and is often not clear when each should be used [5.6]. Depending on their alloying composition and heat treated condition, ferrous alloys can have different hardening mechanisms. Most carbon equivalent formulae consider carbide formers such as chromium, molybdenum, and vanadium [5.6]. However, the formation of carbides is both temperature and compositionally dependent [5.7]. Additionally, different carbide morphologies form depending on the compositional and thermal conditions in which they (e.g. Cr_7C_6, $Cr_{23}C_6$, VC, V_4C_3, etc.) [5.7]. Most carbon equivalent equations are weighted averages which do not consider temperature or the relationship between alloying elements.

Generally, preheating is recommended for ferrous alloys with carbon equivalent values of over 0.35 [5.8]. This study has shown that 30MnVS6, which has a carbon equivalent of 0.60, can be welded without the propagation of cold cracks. Although the hardness of the 30MnVS6 heat affected zone was higher than that of the Jominy end quench test data, this did not appear to have a negative impact on weld performance during fatigue testing. The preheating recommendation for ferrous alloys with carbon equivalents greater than 0.35 should be reconsidered based on this study since the

removal of unnecessary preheating processes could reduce manufacturing cost and improve process efficiency.

5.3 Defect Generation and Quantification

In order to better understand the structural integrity of the welds produced, microstructural and visual inspections were necessary to determine whether or not defects such as cracks or voids were present. Metallurgical inspection concluded internal macrostructural defects were observed in the samples produced using the most extreme parameter combinations. As shown by a balance between laser power and workpiece speed by Yoo [5.1], the parameter ranges selected for this study were within the window for producing defect-free welds. These observations are promising for the potential use of this joint in automotive applications since no significant fracture initiation sites were present which could result in premature failure of the components. With the selection of wider parameter ranges, defects are likely to be produced and can therefore be studied. By understanding how defects are formed in this particular system, parameter ranges to be avoided during manufacturing determined.

Visual inspection of the welded 30MnVS6/SAE 045 XLF joints concluded that some degree of spatter was present on all samples. In addition to being aesthetically undesirable, weld spatter can have a negative impact on welding equipment optics and applications where cleanliness is critical to product function [5.9]. A method for quantifying generated amounts of spatter should be established in order to further understand its relationship to welding parameters.

5.4 Fatigue Performance of Manufactured Welds

Fatigue testing results (Section 4.2) can be used to conclude that the parameters selected for this laser welding trial were able to successfully produce robust welds. No fractures or failures were observed for the five samples. These findings were consistent with the minimal variation observed in the geometry, hardness, and microstructural morphology observed between samples types. The ability to successfully produce laser welds using a variety of parameter combinations is encouraging for the reliable commercial use of the 30MnVS6 and SAE 045 XLF alloy combination.

5.5 Suggested Directions for Future Work

The testing performed was able to provide promising initial findings with regards to the potential implementation of welds between 30MnVS6 and SAE 045 XLF alloys. The results of this work lead to additional research questions and pathways. We will now highlight some of the most noteworthy directions research in the following sections including the selection of broader parameter ranges (Section 5.5.1), determination of cold cracking susceptibility (Section 5.5.2), grain size analysis of weld microstructures (Section 5.5.3), and establishments of fatigue limits (Section 5.5.4).

5.5.1 Investigation of a Wider Parameter Range

In order to fully understand the optimal range in which successful welding can take place for 30MnVS6 and SAE 045 XLF joints, additional testing is needed. A conservative approach was used during the selection of parameter ranges which failed to provide a significant response in weld properties. This approach was taken in order to avoid potential damage to the equipment and workpiece fixtures that are needed for the commercial production of planetary carriers. A wider parameter range could have provided significant information with regards to potential failure modes and should be pursued in the future. Due to production scheduling constraints on available welding equipment, adjustment of the parameter range after metallurgical analysis was not possible and the entire sample run had to be run in one batch. In future work, it is recommended that a smaller batch is first produced using the widest parameter ranges, and then narrowed down in subsequent sample production runs.

It was determined earlier that defect-free welds in S45C steel can be achieved if the effective heat input is limited from 275 to 435 $J/mm^{0.5} \cdot s^{0.5}$ [5.1]. The parameters in this investigation resulted in an effective heat input ranging from 305 to 325 $J/mm^{0.5} \cdot s^{0.5}$. For future studies, it would be beneficial to expand the range of heat input beyond the 275 to 435 $J/mm^{0.5} \cdot s^{0.5}$ range studied by Yoo et al. in order to observe the formation of defects throughout the sample welds. In order to consider heat inputs beyond these ranges, weld velocities of 1,200 to 2,400 mm/min should be assessed in combination with power levels from 1,100 to 2,800 W. These parameters would allow for the analysis of welds produced with an effective heat input between 250 and 450 $J/mm^{0.5} \cdot s^{0.5}$.

Additionally, future selection of parameter ranges should include a more significant investigation of the focal position variable. Adjustments of this variable should relate more to the thickness of the workpiece (2.5 mm) and should also consider the calculation of the laser beam spot size. Again, workpiece thickness should be increased in order to better assess the influence of welding parameters on weld depth for this alloy combination.

5.5.2 Determination of Cold Cracking Susceptibility

Cold cracking was not observed during microstructural evaluation in any of the samples analyzed. In order to fully assess the susceptibility of cold cracking in welded components, a testing method for this system should be developed which aim to induce cold cracking in a controlled manner such as a gapped-bead-on-plate test [5.10]. This would be valuable for determining whether or not specific parameter combinations increase the risk of cold cracking in welded joints, particularly in materials with high carbon equivalent values (i.e. 30MnVS6).

5.5.3 Grain Sizing Across Weld Microstructures

Microstructures observed throughout the welds ranged from the formation of Widmanstätten ferrite in the SAE 045 XLF heat affected zone to varying sizes of lath martensite in the solidification and 30MnVS6 heat affected zones. We anticipate that the varying size of the lath martensite microstructures would benefit from grain size analysis in order to better understand the hardenability within the solidification and 30MnVs6 heat affected zones. An unexpected discrepancy existed within the 30MnVS6 heat affected zone as the hardness in this region exceeded the maximum hardenability shown by the

Jominy end quench test data performed by the steel supplier. Since water quenching, found in Jominy end quench tests, is significantly more aggressive than that of a weld cooling naturally [5.11], it is unclear as to why the maximum hardenability was higher in the 30MnVS6 heat affected zone then in the Jominy sample. Grain sizing analysis of these zones could help determine if a Hall-Petch relationship is a contributing factor to the unexpected hardness levels present in this region [5.12].

5.5.4 S-N Curve Development and Analysis

S-N curves can provide significant insight into the relationship between loads applied to a component and the number of cycles to failure as shown in other works [5.13–16]. Since the samples produced in this study were created using varying parameters, we chose to not vary loading amplitudes. However, since minimal variation was observed from metallurgical and fatigue testing, sample types not metallurgically analyzed during Phase II can be used for future fatigue testing at varying loads. Torsional fatigue testing can then be performed at varying loads in order to produce an S-N curve which can show the relationship between loading amplitudes and cycles to failure. Due to scheduling constraints on fatigue testing equipment, the testing had to be limited to 2 million cycles per sample. For a more extensive understanding of cycles to failure, it is recommended future samples be cycled for up to 10 million cycles as was done by other authors [5.13–16].

5.6 References

[5.1] Y.-T. Yoo, D.-G. Ahn, K.-B. Ro, S.-W. Song, H.-J. Shin, and K. Im: *J. Mater. Sci.*, 2004, vol. 39, pp. 6117–9.

[5.2] A.P. Tadamalle, Y.P. Reddy, and E. Ramjee: *Adv. Prod. Eng. Manag.*, 2013, vol. 8, pp. 52–60.

[5.3] A.P. Tadamalle, Y.P. Reddy, E. Ramjee, and V.K. Reddy: *Adv. Prod. Eng. Manag.*, 2014, vol. 9, pp. 128–38.

[5.4] F. Malek Ghaini, M.J. Hamedi, M.J. Torkamany, and J. Sabbaghzadeh: *Scr. Mater.*, 2007, vol. 56, pp. 955–8.

[5.5] S. Katayama: in *Handbook of Laser Welding Technologies*, Woodhead Publishing Limited, 2013, pp. 3–15, 47–72.

[5.6] Ş. Talaş: *Mater. Des.*, 2010, vol. 31, pp. 2649–53.

[5.7] M. Maalekian: *IWS Austria*, 2007, vol. 1, pp. 1–36.

[5.8] D.L. Olson, ed.: in *ASM Handbook: Welding, Brazing, and Soldering*, vol. 6, ASM Intl, 1993, pp. 229–48, 756–76, 1083–5.

[5.9] A. Ribolla, G.L. Damoulis, and G.F. Batalha: *J. Mater. Process. Technol.*, 2005, vol. 164–165, pp. 1120–7.

[5.10] A.P. Chakravarti and S.R. Bala: *Weld. Journal, Res. Suppl.*, 1989, p. 1s–8s.

[5.11] T.G. Liščić B, Tensi H., Canale L.: in *Quenching Theory and Technology Second Edition*, 2010, pp. 359–443.

[5.12] N. Hansen: *Scr. Mater.*, 2004, vol. 51, pp. 801–6.

[5.13] N. Farabi, D.L. Chen, J. Li, Y. Zhou, and S.J. Dong: *Mater. Sci. Eng. A*, 2010, vol. 527, pp. 1215–22.

[5.14] C.M. Sonsino: *Int. J. Fatigue*, 2009, vol. 31, pp. 88–101.

[5.15] C. Xie, S. Yang, H. Liu, Q. Zhang, Y. Cao, and Y. Wang: *J. Mater. Eng. Perform.*, 2017, vol. 26, pp. 3794–801.

[5.16] Q.L. Cui, D. Parkes, D. Westerbaan, S.S. Nayak, Y. Zhou, D.C. Saha, D. Liu, F. Goodwin, S. Bhole, and D.L. Chen: *J. Mater. Eng. Perform.*, 2017, vol. 26, pp. 783–91.

APPENDIX A

Sample Manufacturing Parameter Codes and Analysis Matrix

Standardized Order	Run Order	Manufacturing Parameter Codes			Inspection Methods (number of parts analyzed)				
					Non-Destructive		Destructive		
		P-Code	v-Code	f-Code	Visual	Ultrasonic	Phase I Metallurgical	Phase II Metallurgical	Torsional Fatigue
1	17	-1	-1	-1	2	2	1		
2	10	-1	-1	0	2	2		1	
3	11	-1	-1	1	2	2	1		
4	16	-1	0	-1	2	2		1	
5	1	-1	0	0	2	2		1	
6	23	-1	0	1	2	2		1	
7	21	-1	1	-1	2	2	1		1
8	8	-1	1	0	2	2		1	
9	3	-1	1	1	2	2	1		1
10	12	0	-1	-1	2	2		1	
11	24	0	-1	0	2	2		1	
12	7	0	-1	1	2	2		1	
13	20	0	0	-1	2	2		1	
14	25	0	0	0	2	2	1		1
15	2	0	0	1	2	2		1	
16	15	0	1	-1	2	2		1	
17	27	0	1	0	2	2		1	
18	18	0	1	1	2	2		1	
19	5	1	-1	-1	2	2	1		1
20	9	1	-1	0	2	2		1	
21	13	1	-1	1	2	2	1		1
22	26	1	0	-1	2	2		1	
23	4	1	0	0	2	2		1	
24	6	1	0	1	2	2		1	
25	22	1	1	-1	2	2	1		
26	14	1	1	0	2	2		1	
27	19	1	1	1	2	2	1		